

© 2014 Mayank Baranwal.

APPLICATION OF FIELD PROGRAMMABLE ANALOG ARRAYS (FPAAS) TO  
FAST SCANNING PROBE MICROSCOPY

BY

MAYANK BARANWAL

THESIS

Submitted in partial fulfillment of the requirements  
for the degree of Master of Science in Mechanical Engineering  
in the Graduate College of the  
University of Illinois at Urbana-Champaign, 2014

Urbana, Illinois

Adviser:

Professor Srinivasa Salapaka

# Abstract

For a long time, signal processing used to be accomplished by microprocessors and DSPs (Digital Signal Processors). The advent of reconfigurable computing devices, such as Complex Programmable Logic Devices (CPLDs) and Field Programmable Gate Arrays (FPGAs) has given a new dimension to signal processing applications [1] by not only allowing users to customize the hardware to suit the specific requirements but also making high speed applications a possibility, too. More recently, Field Programmable Analog Arrays (FPAAs) have emerged as interesting alternatives to most signal processing based applications [2]. Even though the use of FPAA devices is still limited due to small number of suppliers, a growing interest in using FPAAs for various engineering applications is expected [3]. In this thesis, we exploit the FPAAs to demonstrate their usefulness and ease of implementation in developing fast and robust controllers for an Atomic Force Microscope (AFM) unit.

Atomic Force Microscopes (AFMs) are getting faster. However, video-rate imaging still remains a big challenge to the AFM community [4]. Therefore AFMs are required to have very fast nanopositioning systems. However, high-bandwidth requirement on the positioning system poses fundamental limitations on the image resolution [5]. The resolution of an image depends on the controller's capabilities to attenuate the measurement noises. Tools from robust control theory [6], [7] are employed to not only quantify the measurement noises and parametric uncertainties, but also synthesize the controllers in an optimal setting.

However, implementation of such controllers require electronics that can support high-bandwidth operations. Field Programmable Analog Arrays (FPAAs) [8], which have bandwidth up to 400 kHz, have been employed to demonstrate not only the direct implementation of these controllers in terms of transfer functions, but also high-bandwidth tracking performance, too, when compared to most other commercially available Digital Signal Processors (DSPs). A significant improvement in the closed-loop bandwidth ( $\sim 500Hz$ ) has been demonstrated. A part of the work is dedicated to the Q-control of microcantilevers [9]. Since, cantilevers are second-order flexible structures with high resonant frequencies ( $\sim 50kHz$ ), Q-control of cantilevers requires estimating velocity at resonant frequencies. High-bandwidth advantage of FPAAs can be exploited to achieve the desired Q-control.

*To my grandfather and my mother, for their endless love and support*

# Acknowledgments

First, I would like to sincerely thank my adviser Prof. Srinivasa Salapaka for his patience and guidance. Apart from the knowledge he's been imparting in me through various useful discussions on varied topics ranging all the way from research to the current state of politics, I always admire his humility and positive attitude towards the students. Also, a heartfelt thanks to him for taking care of me when I was going through a stressful phase.

I would also like to express my gratitude to my research colleagues Gayathri, Mashrafi, Yunwen and in particular, Ram for not only being a good friend and helping me out on the research front, but also for taking time out to show my parents around when they were in town.

Graduate life in Urbana-Champaign has been a fun-filled journey and I owe this to my friends Piyush, Pranav, Prakalp, Shishir and Srikant.

All through my stay at UIUC, my family has always supported me through their love and encouragement. It's only fair to thank Almighty for having given me a wonderful family to whom I could always look up to for advice and encouragement.

Last, I would like to extend my deepest regards to some of the greatest teachers and researchers at UIUC for instilling confidence and motivation in me to keep striving for excellence.

# Table of Contents

<b>List of Tables</b> . . . . .	<b>vi</b>
<b>List of Figures</b> . . . . .	<b>vii</b>
<b>List of Abbreviations</b> . . . . .	<b>viii</b>
<b>List of Symbols</b> . . . . .	<b>ix</b>
<b>Chapter 1 Introduction</b> . . . . .	<b>1</b>
<b>Chapter 2 System Description</b> . . . . .	<b>4</b>
2.1 Hardware Description . . . . .	4
2.1.1 Anadigm FPAA . . . . .	4
2.1.2 X-Y Nanopositioning System . . . . .	6
2.1.3 NI-DAQmx PCIe-6361 . . . . .	6
2.2 System Identification . . . . .	7
2.2.1 NI-LabView Swept-Sine Measurement VI . . . . .	7
2.2.2 Piezo stage system identification . . . . .	8
2.2.3 Cantilever system identification . . . . .	11
<b>Chapter 3 Control Design Algorithms for the Nanopositioning System</b> . . . . .	<b>15</b>
3.1 Feedback only control design . . . . .	15
3.2 2-DOF $H_\infty$ control . . . . .	18
3.3 2DOF Model-Matching control . . . . .	19
3.4 2DOF Optimal Robust Model Matching Control . . . . .	21
<b>Chapter 4 Controller Implementation on FPAA and Experimental Results</b> . . . . .	<b>23</b>
4.1 Balanced Realization and Model Reduction . . . . .	23
4.2 1DOF $H_\infty$ control design . . . . .	24
4.3 2DOF $H_\infty$ control design . . . . .	27
4.4 2DOF Model-Matching control . . . . .	30
4.5 2DOF Optimal Robust Model Matching control . . . . .	31
4.5.1 Reduced-order controller for Y-stage . . . . .	32
4.5.2 High-order controller for X-stage . . . . .	32
<b>Chapter 5 Q-Control of Microcantilevers</b> . . . . .	<b>38</b>
5.1 Introduction . . . . .	38
5.2 Velocity estimation using modulation-demodulation approach . . . . .	39
5.3 Q-control implementation on FPAA and Experimental results . . . . .	42
<b>Chapter 6 Conclusion and Future Work</b> . . . . .	<b>44</b>
<b>References</b> . . . . .	<b>45</b>

# List of Tables

2.1 Qualitative comparison of reconfigurable technologies . . . . . 5

# List of Figures

2.1	Control system set-up for the flexure stage . . . . .	5
2.2	A custom designed PCB for interfacing FPAA with the AFM . . . . .	6
2.3	Piezo driven flexure 2DOF scanner in an AFM . . . . .	7
2.4	NI PCIe-6361 . . . . .	8
2.5	System identification for the X-stage using Swept-Sine Measurement VI . . . . .	9
2.6	Frequency response results for the piezo-stages . . . . .	10
2.7	Schematic of AFM showing all the fundamental components. In the pictured configuration, both vertical and lateral piezos are located in the base or scanning stage. . . . .	12
2.8	Frequency response results for the cantilever subsystem . . . . .	14
3.1	Schematic of feedback only control design . . . . .	16
3.2	Generalized plant for 1DOF $H_\infty$ -control design . . . . .	16
3.3	A 2DOF control architecture . . . . .	18
3.4	Generalized plant for 2DOF $H_\infty$ control . . . . .	18
3.5	Model matching through the prefilter problem . . . . .	19
3.6	A 2DOF optimal robust model matching control design . . . . .	22
3.7	Generalized plant for optimal 2DOF robust model matching controller . . . . .	22
4.1	Experimental setup for controlling the nanopositioning system . . . . .	24
4.2	Theoretical $S$ and $T$ for 1DOF $H_\infty$ control . . . . .	25
4.3	Designing reduced order feedback controller on an FPAA using AnadigmDesiner2 software . . . . .	25
4.4	Tracking performance using a 1DOF $H_\infty$ -control design . . . . .	26
4.5	Choice of $W_r$ and $W_n$ weighting functions . . . . .	27
4.6	$S$ and $T$ for mixed-sensitivty 2DOF $H_\infty$ control . . . . .	28
4.7	Tracking performance using a 2DOF $H_\infty$ -control design . . . . .	29
4.8	$S$ and $T$ for model-matching control . . . . .	30
4.9	Tracking performance using a 2DOF optimal prefilter based design . . . . .	31
4.10	$S$ and $T$ for model-matching control . . . . .	32
4.11	$S$ and $T$ for optimal robust 2DOF $H_\infty$ loop-shaping controller for the Y-stage . . . . .	33
4.12	Tracking performance using a 2DOF optimal robust $H_\infty$ loopshaping control for the Y-stage . . . . .	34
4.13	Daisy chaining two FPAAs to implement higher-order controller . . . . .	35
4.14	Tracking performance using a 2DOF optimal robust $H_\infty$ loopshaping control for the X-stage . . . . .	36
4.15	$S$ and $T$ for optimal robust 2DOF $H_\infty$ loop-shaping controller for the X-stage . . . . .	37
5.1	Schematic for velocity estimation . . . . .	40
5.2	Implementing Modulation-Demodulation on FPAA . . . . .	41
5.3	Schematic of Q-factor control of a microcantilever . . . . .	42
5.4	Estimating velocity using modulation-demodulation approach . . . . .	43

# List of Abbreviations

AFM	Atomic Force Microscope
CPLD	Complex Programmable Logic Device
DOF	Degree Of Freedom
DSP	Digital Signal Processor
DTFT	Discrete-Time Fourier Transform
FPAA	Field Programmable Analog Array
FPGA	Field Programmable Gate Array
NI	National Instruments
PID	Proportional Integral Derivative
PSD	Power Spectral Density
SPM	Scanning Probe Microscope
TITO	Two-Input-Two-Output

# List of Symbols

Symbol	Description
$G(s)$	Plant transfer function
$P(s)$	Generalized Plant transfer function
$G_{xx}(s)$	X-stage transfer function
$G_{yy}(s)$	Y-stage transfer function
$G_{zz}(s)$	Z-stage transfer function
$G_{dd}(s)$	Dither to Deflection transfer function
$G_{zd}(s)$	Z-piezo to Deflection transfer function
$K_{fb}(s)$	Feedback controller transfer function
$K_{ff}(s)$	Feedforward controller transfer function
$K_{pre}(s)$	Prefilter transfer function
$S(s)$	Sensitivity transfer function
$T(s)$	Complementary Sensitivity transfer function
$e$	Tracking error
$n$	Measurement error
$d$	External disturbance

Symbol	Description
$u$	Control input
$r$	Reference input
$w$	Exogenous input
$z$	Regulated output
$v$	Regulated output
$y$	Sensor output
$W_s(s)$	Sensitivity weighting transfer function
$W_t(s)$	Complementary Sensitivity weighting transfer function
$W_u(s)$	Control weighting transfer function
$T_{ref}(s)$	Reference transfer function
$AM - AFM$	Amplitude Modulation AFM
$Q$	Quality factor
$\omega_n$	Natural frequency

# Chapter 1

## Introduction

Having described the advantages with an FPAA device, the aim of this thesis is to highlight two main components: (a) Control design to improve the bandwidth and tracking performance of a 2-DOF nanopositioning system used in Atomic Force Microscopes (AFMs), and (b) Control implementation on a Field Programmable Analog Array (FPAA). We use tools from robust control theory to design and implement 2DOF controllers for the nanopositioning system. The implementation of higher-order model-based controllers on FPAAs has results in significant improvement in tracking bandwidths when compared to implementing similar control algorithms on a DSP hardware as in [5, 10], mainly due to the low sampling rate constraints and limited number of resources. Moreover, more complex functions such as multiplying signals and generating sinusoidal signals to achieve Q-control of high resonant frequency ( $\sim 50\text{kHz}$ ) cantilevers has been successfully achieved using high-bandwidth advantage of FPAAs.

A typical nanopositioning system used in a Scanning Probe Microscope (SPM) is comprised of a flexure stage, and actuators (typically piezoelectric) and/or sensors along with the feedback system. A systems viewpoint of the nanopositioning system is presented. The main goals of the control design are to achieve high position tracking bandwidth, resolution, and robustness to modeling and environmental uncertainties. The framework used to analyze and control the precision systems is quite general and can be easily extended to other systems as in [11].

It has been a common practice to design Proportional Integral Derivative (PID) controllers for such systems as they are easily implementable. However, the PID controller design does not offer flexibility in design, robust stability property, high bandwidth and high resolution. Also, PID controllers require the gains to be manually tuned without offering much insight into robustness.

This work exploits the control design tools developed for positioning systems in SPM earlier [12]. However, the controllers have been implemented on an FPAA [8]. FPAA offers not only design and implementation of very high bandwidth controllers ( $\sim 400\text{kHz}$ ), but their direct realization in terms of transfer functions. 1DOF  $H_\infty$  control of positioning system using FPAA has been demonstrated earlier in [13]. However, the aim of this thesis is to highlight the significance of 2DOF control over 1DOF control and simultaneously implement

higher order 2DOF controllers using FPAA. For instance, Glover-McFarlane control design [5, 14] has resulted in better repeatability of tracking performance of the nanopositioning systems than feedback only control. In Glover-McFarlane control design, an add-on controller block is wrapped around an existing controller, thereby making the nanopositioning system insensitive to external disturbances, modeling uncertainties and sensor noise. Similarly, a 2DOF  $H_\infty$  control design with both *feedforward* and *feedback* controllers shows significant improvement over the *feedback only* design as in the 2DOF setup, the reference signal gets prefiltered before being fed to the original plant, thereby providing an additional degree to the system.

In SPMs, microcantilevers are used to extract sample topographical information. Q-factor of a microcantilever is the measure of its sensitivity. Equivalently, Q-factor characterizes the bandwidth of a cantilever around the center (resonant) frequency. Cantilever dynamics play an important role in Tapping mode AFM (AM-AFM) [15]. Higher Q-factor corresponds to high-sensitivity of cantilevers and low tip-sample interaction force and is more suitable for biological samples, whereas, low Q-factor allows faster scans with limited resolution. A normal microcantilever has resonant frequency in the orders of few hundreds of kHz. High-bandwidth advantage with FPAAs can be exploited to achieve the desired Q-control.

This thesis shows the design and implementation of four different control algorithms namely the 1DOF  $H_\infty$  design, 2DOF  $H_\infty$  design, Model-matching control design and Glover-McFarlane control design for the X-Y positioning stages in an AFM. In addition, the control hardware is the Analog Field Programmable Analog Array (FPAA) hardware combined with MFP-3D AFM. The 2DOF control designs when implemented on the AFM have given substantial improvements in bandwidth (as high as 480Hz) for the same resolution and robustness. Other performance objectives can be improved by appropriately designing the weight function or target transfer function. This thesis also shows how to estimate cantilever tip-velocity for achieving desired Q-control. Cantilevers are flexible structures with relatively sharper resonant frequencies. Hence, the velocity signal is orthogonal to the deflection signal with the same resonant frequency. Orthogonal signal of a given  $\sim 50\text{kHz}$  signal has been experimentally demonstrated in this work.

Improvements in the tracking performance of the nanopositioning system and the corresponding Q-factor control of the microcantilever would mean faster scan rate and hence, video-rate imaging. Novel research and study of biological processes would then be possible with this added capability of the AFM hardware. A low-resolution video imaging of walking Myosin has been reported in [4]. With the advantage of robust control theory to be able to quantify the resolution and bandwidth, fast controllers with specified resolution can be easily designed and implemented.

The organization of this thesis is as follows. Chapter 2 describes the system details of the AFM and the FPAA hardware, system identification of the positioning system and other subsystems, model fitting

and model reduction. Chapter 3 describes the design of various controllers - 1DOF  $H_\infty$ , 2DOF  $H_\infty$ , Model-matching and Glover-McFarlane controllers. Chapter 4 showcases implementation of aforementioned controllers onto FPAA hardware and discusses the experimental and simulation results. Chapter 5 discusses the setup for Q-control of microcantilevers and discusses the experimental results. This is followed by discussion on further extension of this work.

# Chapter 2

## System Description

### 2.1 Hardware Description

#### 2.1.1 Anadigm FPAA

Reconfigurable computing (FPAAs and FPGAs) has provided solutions to countless engineering problems. For most signal processing applications, FPAAs are clearly the most suited alternatives when compared to their digital counterparts - FPGAs. With the use of floating-gate devices in the core element in the programmable signal processing FPAA [16], this technology offers integration of a larger number of elements per chip, high precision and high efficiency gain when compared to DSP processors.

A brief comparison of the FPAA and the FPGA technologies has been presented in [17]. Regarding the expressiveness of the transfer function models in the reconfigurable devices, the FPAA approach, because of its analog implementation, is closer to mathematical models than the FPGA approach, which doesn't exactly portray the exact mathematical model because of the  $Z$ -transform and quantization. Moreover, FPGAs demand sound understanding of system resources and allocation, etc. In contrast, filter-design in FPAAs thrives on simple op-amps based circuit that can be easily configured using the provided development tools and software. Moreover, FPAA devices are cheaper than their digital counterparts. Moreover, the FPAAs supplied by Anadigm [8] has the advantage of having multiple functional blocks ready to use and, therefore, the analog implementation is straightforward.

Although, a direct comparison is not possible, current FPGA devices seem to have larger device capacity than the FPAA devices. However, two FPAAs can be used in series to implement up to a sixteenth-order analog filter. The maximum operation frequency of the devices may limit their use in some applications. The Anadigm FPAA used in this thesis runs at 16 MHz and can process signals up to 2 MHz. FPGAs, on the other hand can operate at much higher frequencies (500 MHz). However, this is severely constrained by the optimization and implementation done by the design software. All the above aspects of FPAA devices make them preferred choice for control systems application. In the context of the desired control systems

Table 2.1: Qualitative comparison of reconfigurable technologies

Design Parameter	FPAA	FPGA
Ease of Implementation for control systems application	+++	-
Design Tools and Software	+++	++
Cost	+++	+
Performance	+++	+++
Capacity	+	++
Running Frequency	+	+++
Gain	+	++
Power Consumption	-	+
	+++ excellent	++ good
		+ average
		- weak

application to an AFM, this comparison can be summarized as:

The control design is implemented on an Anadigm FPAA [18] using AnadigmDesigner2 EDA software. Field programmable analog arrays (FPAAs) from Anadigm give an analog equivalent to the FPGA, thereby allowing design of complex analog signal processing functions into an integrated, drift-free, pre-tested device. The set-up of the control system is shown in Fig. 2.1.

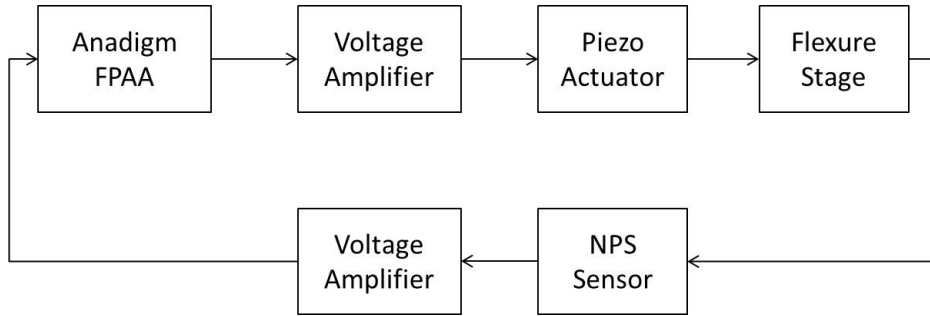


Figure 2.1: Control system set-up for the flexure stage

FPAA [8] offers direct realization of very high bandwidth controllers ( $\sim 400kHZ$ ) by employing AnadigmDesigner2 EDA software. The software allows designer to construct complex analog functions using configurable analog modules (CAMs) as building blocks. With easy-to-use drag-and-drop interface, the design process can be measured in minutes allowing complete analog systems to be built rapidly, simulated immediately, and then downloaded to the FPAA chip for testing and validation. A custom designed PCB (see Fig. 2.2) is used to interface single-ended 10V AFM signals with 0 – 3.3V differential signals referenced at 1.5V. This is achieved by using operational amplifiers AD-8130 and AD-8132 (Analog Devices, Norwood, MA, USA) to scale and convert differential signals to single-ended signals and vice versa. Even though FPAA offers very high flexibility in terms of designing and implementing high-order, high-bandwidth controllers; it is relatively more sensitive to electrical noises when compared to its digital counterpart - FPGA. Also, the



Figure 2.2: A custom designed PCB for interfacing FPAA with the AFM

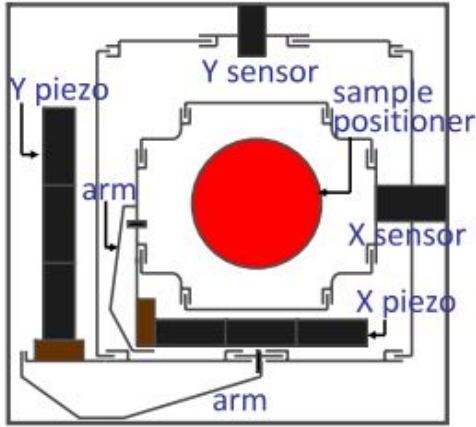
CAMs can't be configured very accurately to model an exact given transfer function. This may result in a slightly different control design than expected. However, this effect is usually very small and can be ignored in most cases.

### 2.1.2 X-Y Nanopositioning System

A schematic of the X-Y nanopositioning system (MFP-3D X-Y scanner) is shown in Fig. 2.3. The scanner has two flexure components with component 'X' stacked over the 'Y' where the sample holder is carried by the X-component. Both stages can deform under the application of force, thereby providing the required motion. These forces are generated using stacked-piezos. There are three piezoactuators in series for each axis. The motion of each flexure component is measured by the corresponding nanopositioning sensors which are modified from the linear variable differential transformer (LVDT) and the associated demodulation circuit. The piezoactuators lead to a travel range of  $90\mu m$  in a closed loop in both directions. The nanopositioning sensors have noise less than  $0.6nm$  (deviation) over  $0.1 - 1kHz$  bandwidth.

### 2.1.3 NI-DAQmx PCIe-6361

NI PCIe-6361 (Fig. 2.4) is an X series multifunction data acquisition (DAQ) device with high-throughput PCI Express bus, NI-STC3 timing synchronization technology, and multicore-optimized driver. The device



(a) Schematic of a flexure scanner



(b) MFP-3D X-Y scanner

Figure 2.3: Piezo driven flexure 2DOF scanner in an AFM

has 16-bits ADCs (Analog to Digital Converters) and DACs (Digital to Analog Converters) with multi-channel sampling rate up to  $1\text{MS/s}$ . The device is used not only to generate reference signal but also to acquire stimulus and response signals required during system identification.

## 2.2 System Identification

In general, it is near to impossible to come up with accurate mathematical models of the various subsystems of an AFM system using basic laws of physics. Hence, an experimental approach was adapted to determine mathematical models of such complex subsystems. The method is the well-known blackbox identification method where the system is modeled without looking into the internal structure or dynamics of the system [19]. A chirp signal is provided to the system and the output is measured. The chirp signal is particularly useful because the frequencies that are put through the system are directly specified, while using a limited amount of data. Everything in between the input signal and the output signal is considered as the black-box. A linear parametric model is then fitted to this experimental input-output data.

### 2.2.1 NI-LabView Swept-Sine Measurement VI

Commercially available Dynamic Signal Analyzers (DSAs) such as Agilent 35670A FFT Dynamic Signal Analyzer can be used to generate chirp signal (swept-sine signal) and simultaneously analyze the corresponding response signal. However, such devices are expensive and fail to perform identification beyond  $51.2\text{ kHz}$ . In this thesis, we use NI PCIe-6361 board to acquire and generate signals. Since, the board can support a maximum of  $1\text{ MS/s}$  (Mega samples per second) for multi-channel operation, by Nyquist limit;



Figure 2.4: NI PCIe-6361

the identification can be performed up to a theoretical maximum of 500 kHz. This is a significantly better than commercially available DSAs.

We use the ‘NI Swept-Sine Measurement’ example to measure the frequency response and harmonic distortion of a device under test (DUT). Identification up to 300 kHz has been experimentally demonstrated in this thesis. Fig. 2.5 shows frequency response measurements for the nanopositioning system using NI PCIe-6361 and Swept-Sine Measurement VI.

### 2.2.2 Piezo stage system identification

The chirp-signal based system identification yields following results for the the three stages - X, Y and Z (see Fig. 2.6): Clearly, the positioning piezos’ bandwidth is approximately 1 kHz. We are anyway not interested in the dynamics beyond this frequency regime. MATLAB `invreqs` command is used to fit a linear parametric model through the frequency response data. Weighted iterative least square fitting was performed

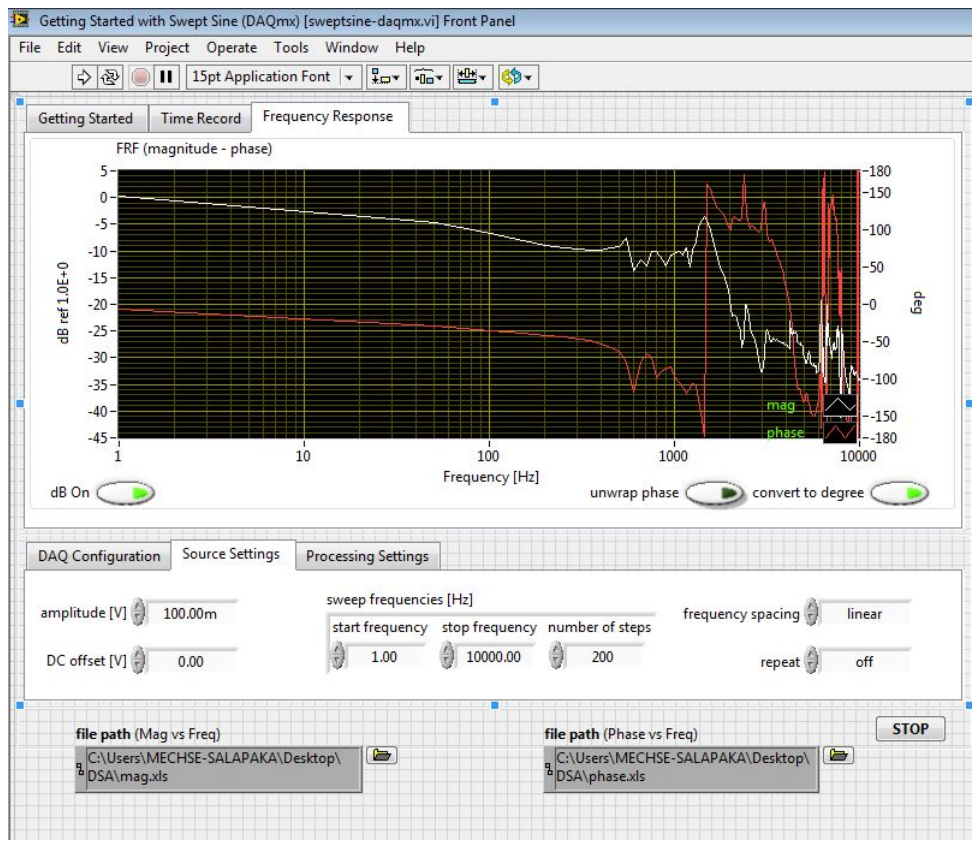
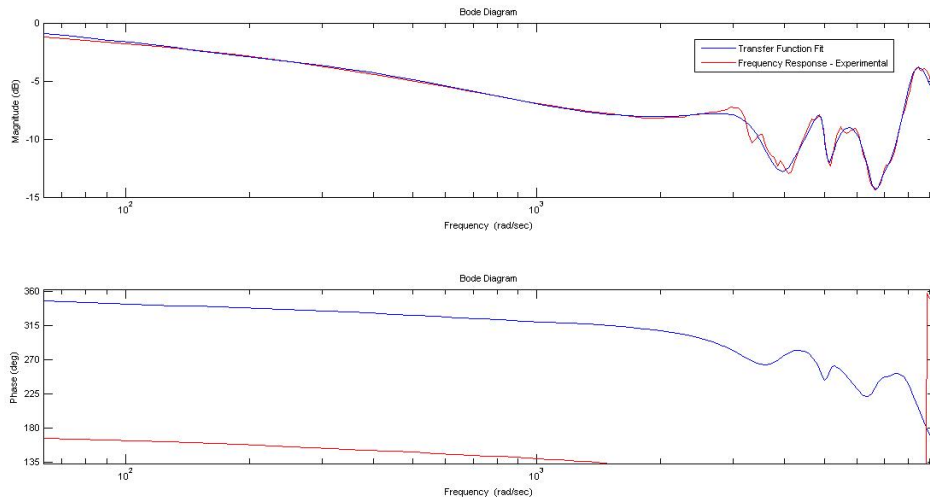
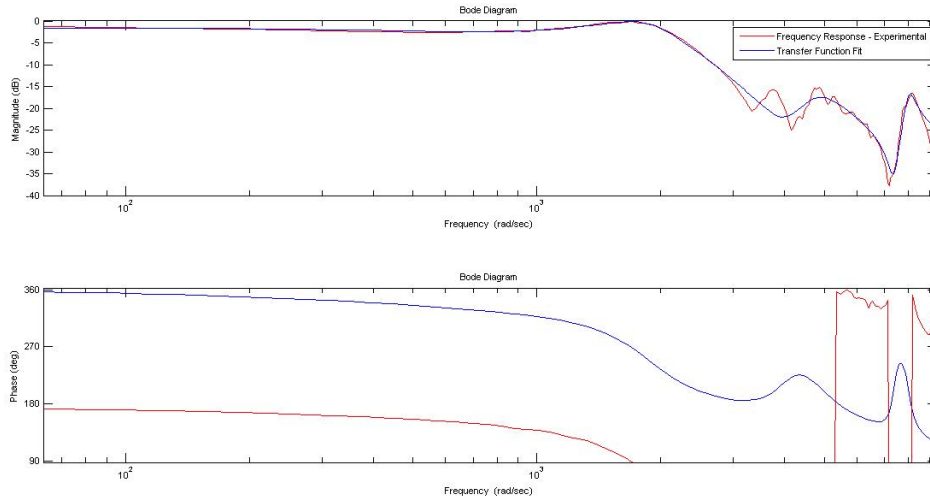


Figure 2.5: System identification for the X-stage using Swept-Sine Measurement VI

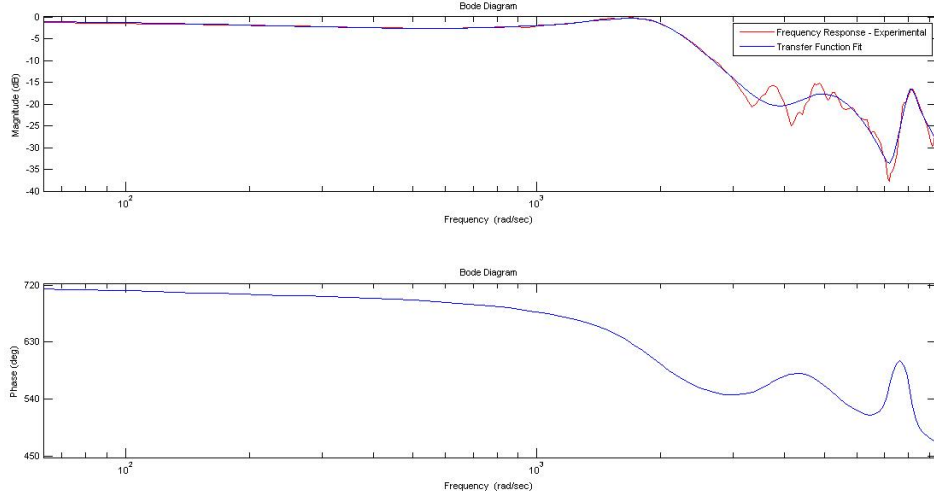


(a) X-stage frequency response



(b) Y-stage frequency response

Figure 2.6: Frequency response results for the piezo-stages



(c) Z-stage frequency response

Figure 2.6: (cont.) Frequency response results for the piezo-stages

over 0-2kHz and the reduction through balanced realization [6] resulted in the following parametric models:

$$\begin{aligned}
 G_{xx} &= \frac{-0.022119(s + 2.954 \times 10^4)(s + 8117)(s - 8151)(s + 418.9)(s^2 + 890.2s + 1.131 \times 10^7)}{(s + 1796)(s + 217.1)(s^2 + 717.5s + 1.013 \times 10^7)(s^2 + 1827s + 3.751 \times 10^7)} \\
 &\times \frac{(s^2 + 1185s + 4.616 \times 10^7)(s^2 + 350.3s + 1.175 \times 10^8)(s^2 + 452.4s + 1.494 \times 10^8)}{(s^2 + 1440s + 7.142 \times 10^7)(s^2 + 267.1s + 1.182 \times 10^8)(s^2 + 605.8s + 1.473 \times 10^8)} \quad (2.2.1)
 \end{aligned}$$

$$\begin{aligned}
 G_{yy} &= \frac{0.025231(s + 1329)(s^2 + 1008s + 1.673 \times 10^7)}{(s + 738.8)(s^2 + 981.1s + 3.574 \times 10^6)} \\
 &\times \frac{(s^2 + 508s + 5.426 \times 10^7)(s^2 - 1.172 \times 10^4s + 1.097 \times 10^8)}{(s^2 + 1213s + 2.35 \times 10^7)(s^2 + 483.8s + 6.512 \times 10^7)} \quad (2.2.2)
 \end{aligned}$$

$$\begin{aligned}
 G_{zz} &= \frac{-0.17329(s - 2.174 \times 10^4)(s^2 + 241.8s + 4.317 \times 10^7)(s^2 + 855.5s + 1.001 \times 10^8)}{(s + 1.347 \times 10^4)(s^2 + 125s + 4.333 \times 10^7)(s^2 + 640s + 9.771 \times 10^7)} \\
 &\times \frac{(s^2 + 709.8s + 2.279 \times 10^8)(s^2 + 3864s + 5.538 \times 10^8)}{(s^2 + 1140s + 1.933 \times 10^8)(s^2 + 717.7s + 2.338 \times 10^8)} \quad (2.2.3)
 \end{aligned}$$

### 2.2.3 Cantilever system identification

A schematic of the components fundamental to AFM operation is shown in Fig. 2.7. The “brain” of the AFM is located in the AFM head. A cantilever with an extremely sharp tip is mounted at the bottom of the head. Every variation of the surface height varies the force acting on the tip and therefore varies the bending of the cantilever. This bending is measured by a sensing mechanism located in the AFM head. The sensing mechanism comprises of a laser beam incident on the cantilever and reflected onto a split photo-sensitive

diode (PSD). Deflection of the cantilever owing to tip-sample interactions results in change of laser incidence angle, which is captured by change in location of the laser spot on the PSD. The base of the cantilever is

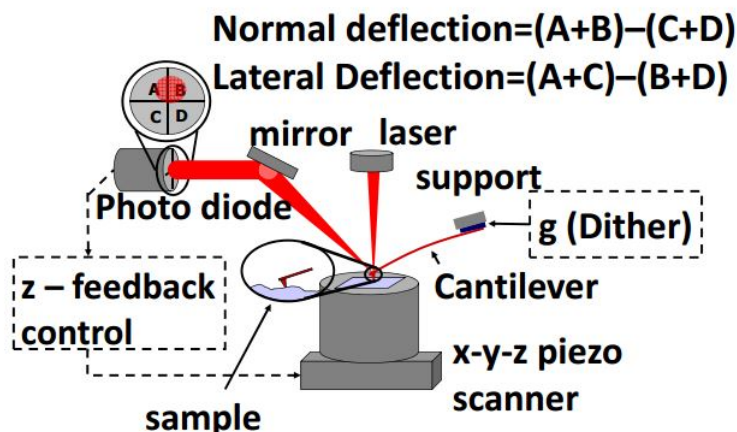


Figure 2.7: Schematic of AFM showing all the fundamental components. In the pictured configuration, both vertical and lateral piezos are located in the base or scanning stage.

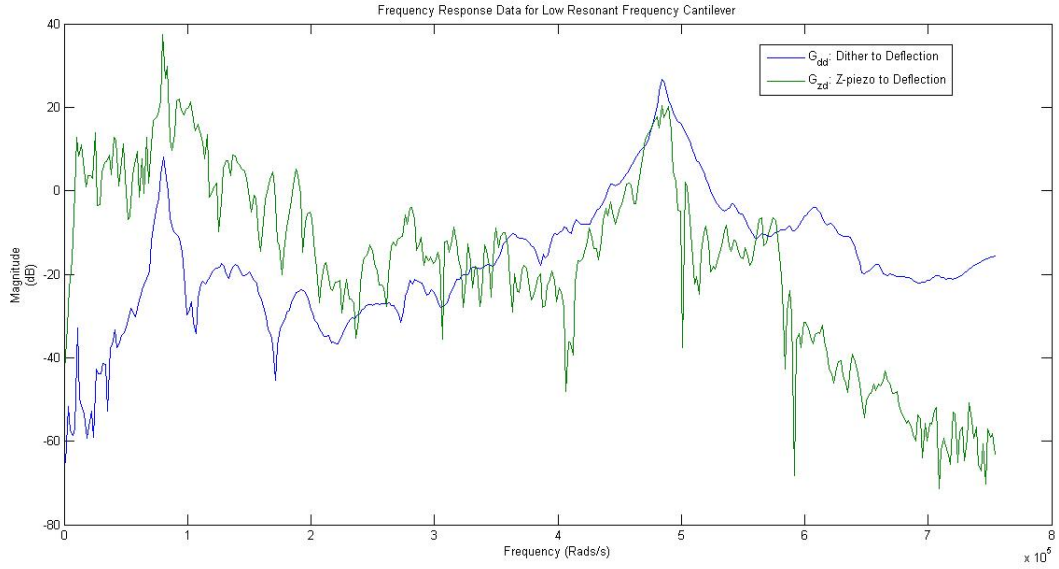
attached to a dither piezo also called as the shake piezo. During dynamic scans, the dither piezo is used to oscillate the cantilever sinusoidally. This piezo typically has very high bandwidths in the order of 600 kHz to accommodate similar orders of cantilever resonance frequencies. Also, the Z-piezo actuator is located along with the cantilever and the laser optic arrangement, in the AFM head. As a result, the Z-piezo actuation causes vertical movement of the cantilever along with its base. Typical travel for the z piezo is around  $15\mu\text{m}$ .

The type of setup for the AFM allows the movement of cantilever tip through not only dither piezo but Z-piezo too. Typical dynamic imaging modes rely only on the dither piezo to produce a set-amplitude sinusoidal actuation of the cantilever tip and measure the change in amplitude to accordingly vertically actuate the cantilever arrangement using Z-piezo. This mode of imaging typically requires several cycles to measure the amplitude change and is a hindrance to video-rate imaging. A new form of dynamic mode imaging has been proposed in [20], that uses the Z-piezo as a low bandwidth controller and the dither piezo as a high bandwidth controller for controlling the cantilever deflection, thereby eliminating the need to wait for several cycles to measure the amplitude change.

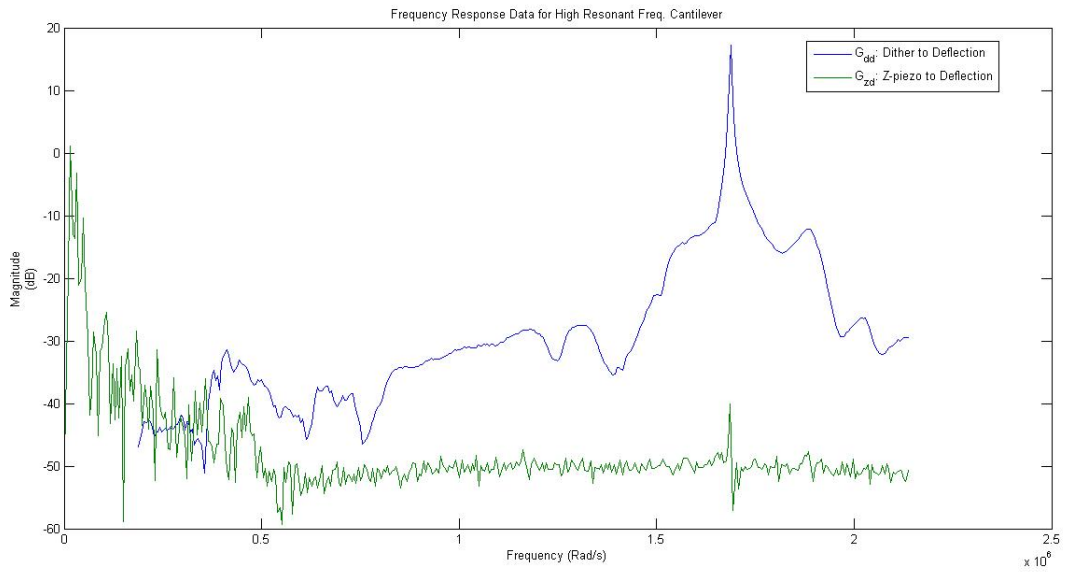
Hence, the cantilever subsystem is viewed as a TITO (Two-Input-Two-Output) system in which the low-voltage signals to the dither and Z piezos are the inputs and the cantilever ‘Deflection’ and ‘Z sensor’ are the outputs. This results in four input-output transfer functions  $G_{dd}$ ,  $G_{zd}$ ,  $G_{zz}$  and  $G_{dz}$ . By virtue of the AFM head design; there is hardly any change in the Z-sensor measurements by actuating the dither piezo. Therefore,  $G_{dz} \approx 0$  for all practical purposes. Also,  $G_{zz}$  is independent of the choice of cantilever and has

been identified in the previous section. The identification was performed for two different cantilevers - low frequency (1<sup>st</sup> mode:  $\sim 12.6$  kHz, 2<sup>nd</sup> mode:  $\sim 76.3$  kHz); and high frequency (1<sup>st</sup> mode:  $\sim 270$  kHz). Fig. 2.8 shows the experimental frequency response results for the two cantilevers.

It can be seen that for the high resonant frequency cantilever,  $G_{zd} \approx 0$  with a very small but observable peak at the resonant frequency 270 kHz. The reason being that the Z-piezo has limited bandwidth ( $\sim 10$  kHz) and dither-to-deflection amplification for this cantilever is almost non-existent in the low frequency regime. The deflection signal has significant amplification only near the resonant frequency at 270 kHz, thereby making deflection signal insensitive to Z-piezo actuation. This also limits the choice of cantilevers that can be used to image samples using the approach described in [20].



(a) Frequency response data for low-frequency cantilever



(b) Frequency response data for high-frequency cantilever

Figure 2.8: Frequency response results for the cantilever subsystem

## Chapter 3

# Control Design Algorithms for the Nanopositioning System

The nanopositioning system comes with a tunable PI only controller with a maximum scan rate of 1 Hz. The most common approach to increasing tracking bandwidth is to increase the resonance frequency of a nanopositioning system by building devices that are sufficiently stiff and small. However, building small scanning devices limits the maximum traversal of the system to a few microns. The work in this thesis is focused on designing and implementing high-end controllers giving robust stability, high bandwidth, high resolution, disturbance rejection and noise attenuation without changing the basic design of the flexure stage.

There have been several approaches to improve the resolution and accuracy of the positioning system. These include - feedforward implementation [21, 22]; using charge amplifiers instead of voltage amplifiers to reduce hysteresis [23]; and feedback control designs with large gains at low frequencies [24, 25]. The feedback control framework presented in [25] uses the tools from robust control theory to determine and quantify the trade-offs between performance objectives and assess if it's feasible to design a controller, given the desired specifications. Most recently, 2DOF control design framework [26, 27, 28] is being employed where the regular feedback control is appended with a feedforward scheme for the reference signal. 2DOF control design which deals with the reference and the measured output signal separately has better capability to satisfy robustness and performance objectives.

This thesis presents control design for the Y-stage using - 1) 1DOF  $H_\infty$  framework, 2) 1DOF  $H_\infty$  framework, 3) 2DOF Model-Matching framework and 4) 2DOF Glover-McFarlane robustifying framework. The shortcomings of the 1DOF control design can be seen to be successfully eliminated in the 2DOF setup. The details of the various control designs are as follows:

### 3.1 Feedback only control design

Fig. 3.1 shows the schematic of a 1DOF (Feedback only) control design.

Instead of designing a tunable PI/PID filter for the feedback control, which doesn't offer much insights into the closed-loop system stability and robustness issues, a 1DOF  $H_\infty$  control framework is presented. The

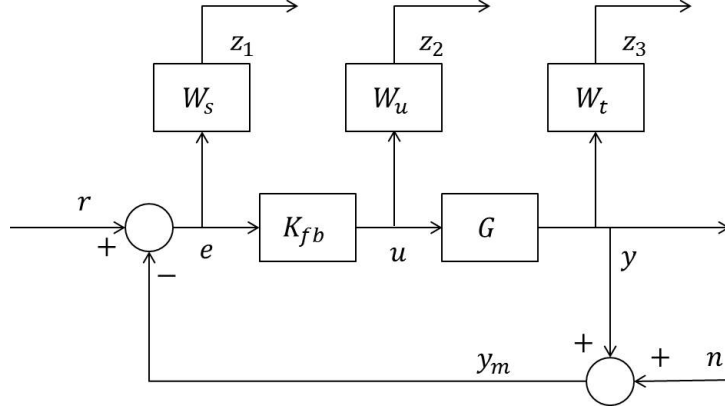


Figure 3.1: Schematic of feedback only control design

performance and robustness objectives can be directly specified by specifying requirements on the ‘sensitivity’ and the ‘complementary sensitivity’ transfer functions. Fig. 3.2 shows a generalized plant for 1DOF  $H_\infty$  control design framework.

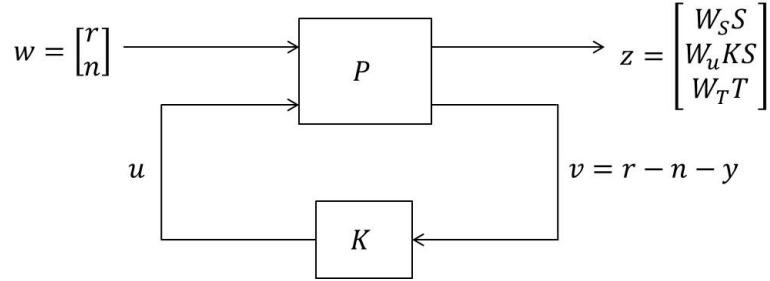


Figure 3.2: Generalized plant for 1DOF  $H_\infty$ -control design

From Fig. 3.2,

$$e = r - y - n = r - G.u - n = r - GKe - n \quad (3.1.1)$$

$$e = (1 + GK)^{-1}(r - n) = S(r - n) \quad (3.1.2)$$

$$y = GKe = GK.(1 + GK)^{-1}(r - n) = T(r - n) \quad (3.1.3)$$

$$u = Ke = KS(r - n) \quad (3.1.4)$$

$$S = 1/(1 + GK) \quad (3.1.5)$$

$$T = GK/(1 + GK) \quad (3.1.6)$$

$$S + T = 1 \quad (3.1.7)$$

where,  $S$  is the sensitivity transfer function, which is a closed-loop transfer function from reference  $r$  to tracking error  $e$ , and  $T$ , known as the complementary sensitivity transfer function, is the closed-loop transfer function from reference  $r$  to the system output  $y$ .  $S$  can also be represented as  $\frac{dy/y}{dG/G}$  that represents the percentage change in the plant model. Therefore,  $S$  is a measure of robustness of the closed-loop system to modeling and parametric plant uncertainties. A general rule of thumb is to not allow the sensitivity transfer function to have peak value beyond 6 dB, i.e.,

$$\|S\|_{\infty} < 2 \quad (3.1.8)$$

The bandwidth  $\omega_B$  is determined based on the frequency corresponding to the point where Bode plot of the sensitivity transfer function crosses the -3 dB line from below. For larger bandwidth, it is required that  $S$  crosses -3 dB line as later as possible. However, because of the algebraic constraint,  $S + T = 1$ , increasing  $\omega_B$  would mean that  $T$  would still be large for relatively higher frequencies. Because,  $T$  also represents the closed-loop transfer function from noise  $n$  to output  $y$ , this would result in significant amplification of high-frequency noise, thereby resulting in poor tracking performance. Similar to  $\omega_B$ ,  $\omega_{BT}$  is the bandwidth based on the complementary sensitivity transfer function  $T$ , defined by its crossing of the -3 dB line from above. For better resolution, i.e., better noise mitigation,  $\omega_{BT}$  should be small.

Similarly,  $KS$  is the closed-loop transfer function from tracking error  $e$  to controller output  $u$ .  $KS$  needs to be bounded so that the controller output  $u$  is bounded. Since, in case of MFP-3D, the maximum absolute voltage the piezo-actuators can safely handle is  $\sim 10V$ , bounding controller output to avoid controller saturation and device failure is important.

All these design constraints on the various closed-loop transfer functions are specified using inverse weighing functions  $W_s$ ,  $W_u$  and  $W_t$ . The optimization problem then is to solve for all stabilizing controllers  $K$  posed in the stacked sensitivity framework,

$$\min_{K \in \mathcal{K}} \left\| \begin{array}{c} W_s S \\ W_u K S \\ W_t T \end{array} \right\|_{\infty} \quad (3.1.9)$$

where,  $\mathcal{K}$  is a set of all stabilizing controllers.

### 3.2 2-DOF $H_\infty$ control

Because of the various algebraic and design constraints, the feedback only scheme has certain performance limitations, which can be alleviated by using a 2DOF architecture shown in Fig. 3.3.

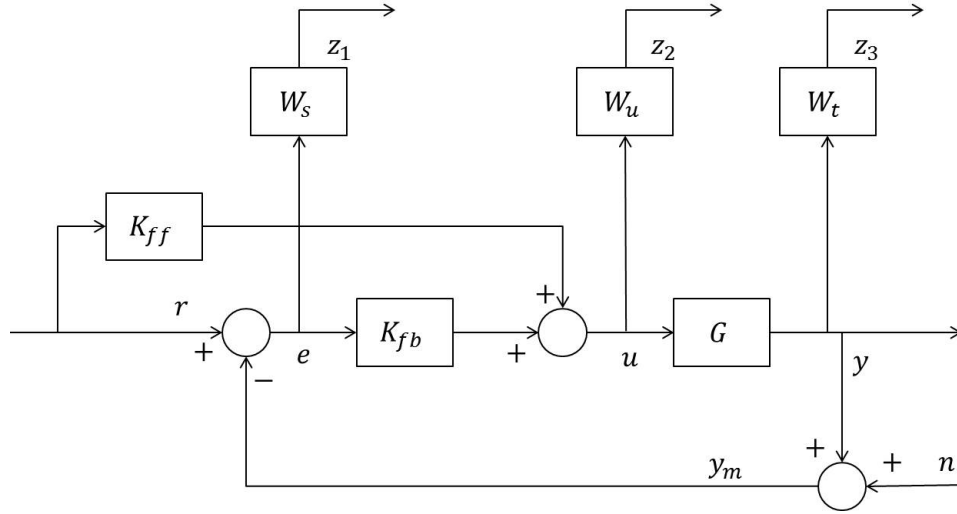


Figure 3.3: A 2DOF control architecture

In contrast to the feedback-only scheme described in previous section, where the controller acts only on the difference between the reference  $r$  and the position-measurement  $y_m$ , in the 2DOF scheme, the controller acts independently on them. The generalized plant for a 2DOF  $H_\infty$  control framework is shown in Fig. 3.4. From the Fig. 3.4,

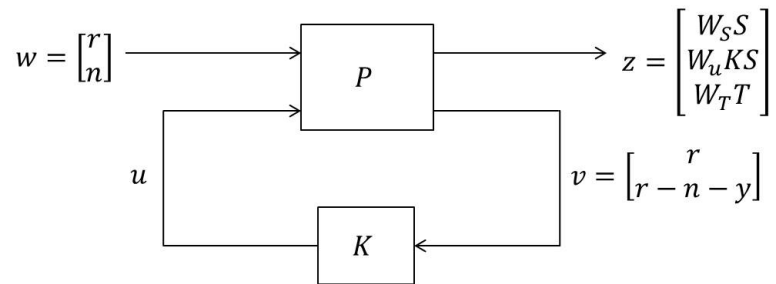


Figure 3.4: Generalized plant for 2DOF  $H_\infty$  control

$$\text{Tracking error, } e = S_{er}r + Tn \quad (3.2.1)$$

$$\text{Position, } y = T_{yr}r - Tn \quad (3.2.2)$$

$$\text{Control (actuation) signal, } u = S(K_{ff} + K_{fb})r - SK_{fb}n \quad (3.2.3)$$

$$S + T = 1 \quad (3.2.4)$$

$$S_{er} = S(1 - GK_{ff}) \quad (3.2.5)$$

$$T_{yr} = SG(K_{ff} + K_{fb}) \quad (3.2.6)$$

The feedback-only control scheme is indeed a special case of the 2DOF scheme, where  $K_{ff} = 0$ . The control objectives translate to small roll-off frequency as well as high roll-off rates for  $T$  to have good resolution, a long range of frequencies for which  $S_{er}$  is small to achieve large bandwidth, and low (near 1) values of the peak in the magnitude plot of  $S(j\omega)$  for robustness to modeling uncertainties. The  $H_\infty$  optimization problem is to find stabilizing controllers  $K = [K_{ff}K_{fb}]^T \in \mathcal{K}$  such that the  $H_\infty$  norm of the regulated output  $z$  is minimized.

### 3.3 2DOF Model-Matching control

Some nanopositioning systems have pre-designed feedback component  $K_{fb}$ , which can't be replaced or changed. However, typically there are no such restrictions on the feedforward control design since it can be easily implemented as a prefilter on the reference signal. The prefilter  $K_{pre}$  is chosen so that the closed loop transfer function  $T$  mimics the reference transfer function  $T_{ref}$  (Fig. 3.5). Desired transient characteristics

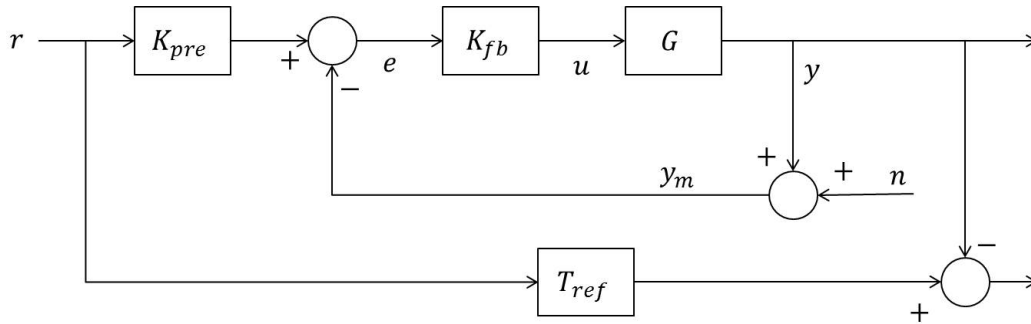


Figure 3.5: Model matching through the prefilter problem

such as settling time and overshoot can be incorporated by choosing the appropriate model  $T_{ref}$ , and since

the closed-loop device is designed to mimic the model, it inherits the transient characteristics too. If  $T$  is the original complementary sensitivity transfer function with the feedback only component, the mismatch error signal from the Fig. 3.5 is given by,

$$\begin{aligned} e &= T_{ref}r - y \\ &= (T_{ref} - TK_{pre})r \end{aligned} \quad (3.3.1)$$

Hence from eq. 3.3.1, minimizing the mismatch error signal is equivalent to,

$$\min_{K_{pre} \in \mathcal{K}} \|E(s)\|_{\infty} = \min_{K_{pre} \in \mathcal{K}} \|T - TK_{pre}\|_{\infty} \quad (3.3.2)$$

where,  $\mathcal{K}$  is a set of all stabilizing controllers

If  $T$  is minimum phase with RHP (right half plane) zeros, this optimization problem is trivial and the optimal prefilter,  $K_{pre} = T^{-1}T_{ref}$ . However, typical nanopositioning systems are flexure based with non-collocated actuators and sensors, which typically manifest as non-minimum phase zeros of  $T$ . In this case, the optimal solution can be found by applying NP (Nevanlinna-Pick) theory described in [29].

This model matching problem is equivalent to finding  $\gamma_{opt}$ ,  $0 < \gamma_{opt} < \gamma$  such that  $\|T - TK_{pre}\|_{\infty} = \gamma_{opt} < \gamma$  for some stable  $K_{pre}$ . By defining  $E_{\gamma} = \frac{1}{\gamma}(T - TK_{pre})$ , the original problem reduces to finding stable  $K_{pre}$  for which  $\|E_{\gamma}\|_{\infty} \leq 1$ . Note that, for stable  $K_{pre}$ ,  $E_{\gamma}$  satisfies the interpolating conditions  $E_{\gamma}(z_i) = \frac{1}{\gamma}T_{ref}(z_i)$  for every RHP zero  $z_i$  of the scanner  $G$ . This is an NP problem to find a function  $E_{\gamma}$  in this space of stable, complex-rational functions such that it interpolates,

$$\{(z_i, E_{\gamma}(z_i))\}_{i=1}^n \quad (3.3.3)$$

Moreover, the optimal value  $\gamma_{opt}$  equals the square root of the largest eigenvalue of the matrix  $A^{-frac{1}{2}}BA^{-frac{1}{2}}$ , where the elements of matrix  $A$  and  $B$  are, respectively

$$a_{ij} = \frac{1}{z_i + \bar{z}_j} \quad (3.3.4)$$

$$b_{ij} = \frac{b_i \bar{b}_j}{z_i + \bar{z}_j} \quad (3.3.5)$$

The optimal stable prefilter,  $K_{pre}$  is then given by,

$$K_{pre} = T^{-1}(T_{ref} - \gamma_{opt}E_{\gamma}) \quad (3.3.6)$$

**Note:** For better tracking, it is important that the closed-loop transfer function  $TK_{pre}$  matches the reference transfer function  $T_{ref}$  at zero-frequency (i.e. the DC gain match). Also, the optimal prefilter obtained using NP solution may not be proper and hence not realizable. So, a weight function  $W_0$ , which is a low-pass filter needs to be multiplied to  $K_{pre}$  so that the weighted prefilter  $W_0K_{pre}$  becomes proper. This prefilter based control may suffer from robustness issues as the optimization problem doesn't account for trade-off between bandwidths and resolutions.

### 3.4 2DOF Optimal Robust Model Matching Control

For some nanopositioning systems, it is critical that the system is robust to modeling uncertainties. Systems with pre-designed feedback controllers may have satisfactory resolution and tracking bandwidth when operated at 'near optimal' operating conditions. However, slight deviation from these operating conditions may result in rapid degradation in tracking performance. Sometimes, this deviation may even result in system instability. For such systems, robustness is a major concern. In [30], Glover-McFarlane method [14, 31] that wrapped around pre-existing controllers were implemented that resulted in significant improvements in robustness. In this thesis, we use a 2DOF control design developed in [32, 33] to simultaneously design a wrap-around feedback controller for robustness as well as the feedforward controller for better bandwidth.

Fig. 3.6 shows the optimal 2DOF robust control architecture. The plant  $G_s = GK_s$  is the shaped plant with  $K_s$  being the pre-existing controller. The optimization routine seeks  $K = [K_r \ K_y]$  such that the closed-loop system guarantees 'optimal' robustness to modeling uncertainties as well as minimizing the mismatch between the transfer function from  $r$  to  $y$  and a reference transfer function  $T_{ref}$ . The robustness condition is imposed by requiring the controller to guarantee stability for a set of transfer function models that are 'close' to the nominal model  $G_s$ . The resulting optimal controller guarantees the stability of the closed-loop positioning system where the shaped plant is represented by *any* transfer function  $G_p$  in the set:

$$\{G_p | G_p = (M - \Delta_M)^{-1}(N + \Delta_N), \text{ where } \|[\Delta_M \ \Delta_N]\|_\infty \leq \gamma^{-1}\} \quad (3.4.1)$$

where,  $G_s = M^{-1}N$  is a coprime factorization [34],  $[\Delta_M \ \Delta_N]$  represents the uncertain dynamics, and  $\gamma$  specifies a bound on this uncertainty.

Fig. 3.7 shows the generalized plant for 2DOF optimal control robust control framework.

The optimal control problem is cast in the  $H_\infty$  framework. The regulated output in this case is  $z = [u^T \ y^T \ e^T]^T$  and the controller  $K$  is sought to minimize the  $H_\infty$  norm of the transfer function  $\Phi_{zw}$  from

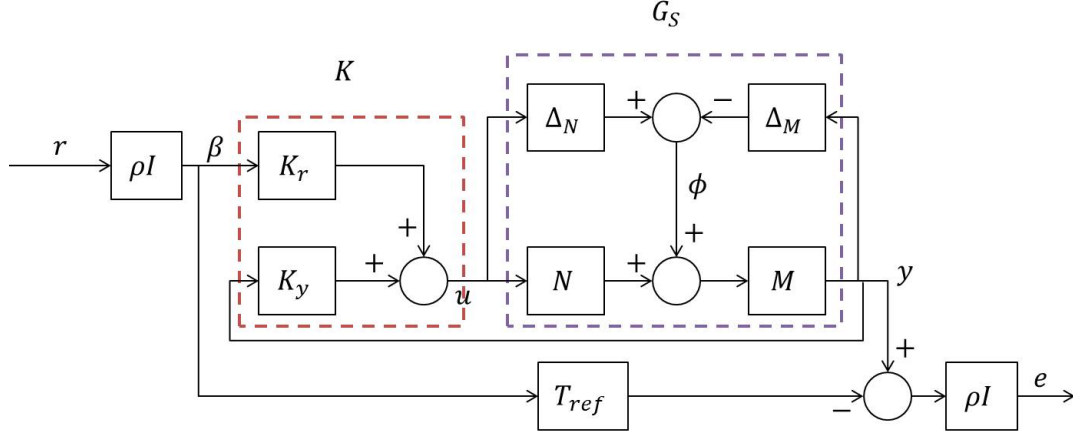


Figure 3.6: A 2DOF optimal robust model matching control design

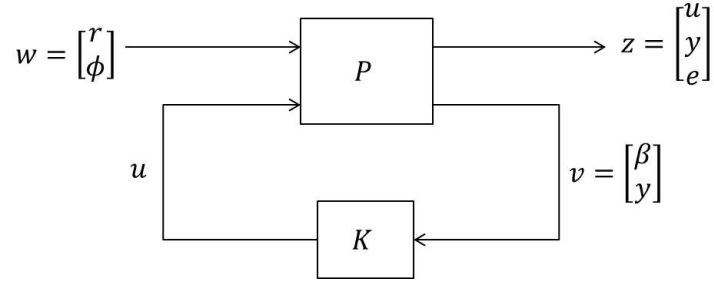


Figure 3.7: Generalized plant for optimal 2DOF robust model matching controller

$w = [r^T \ \phi^T]^T$  to  $z$ , as shown in the Fig. 3.6, described by,

$$\begin{bmatrix} u \\ y \\ e \end{bmatrix} = \begin{bmatrix} \rho K_r S & K_y S M^{-1} \\ \rho G_s K_r S & S M^{-1} \\ \rho^2 (G_s K_r S - M_0) & \rho S M^{-1} \end{bmatrix} \begin{bmatrix} r \\ \phi \end{bmatrix} \quad (3.4.2)$$

where,  $S = (1 - G_s K_y)^{-1}$  and the exogenous signal  $\phi$  represents a disturbance signal due to the unmodeled dynamics.

**Note:** Similar to the prefilter based control design, for better tracking,  $K_r$  needs to be scaled so that the closed-loop transfer function matches the reference transfer function for the steady state problem (i.e., the dc gain match). A scale constant  $W_0$  defined as  $W_0 = S(s)[G_s(s)K_y(s)]^{-1}T_{ref}|_{s=0}$  is multiplied to the original  $K_r$  and the resulting controller becomes  $K = [K_r W_0 \ K_y]$ .

## Chapter 4

# Controller Implementation on FPAA and Experimental Results

### 4.1 Balanced Realization and Model Reduction

A state-space realization with equal and diagonal controllability and observability gramians is called a balanced realization [6]. Assuming the scanner system  $G$  has a state-space realization  $(A, B, C, D)$ , this realization is *minimal* if  $(A, B)$  is *controllable* and  $(C, A)$  is *observable*. Minimal realization is the lowest order realization possible for a given system. The  $A$  matrix of the minimal realization is Hurwitz. Balanced realization is obtained by applying certain state transformation to the minimal realization of the system. A balanced system will have the controllability and observability ellipsoids exactly aligned. Thus the more controllable states are also more observable.

Balanced realization usually comes as a precursor step of model reduction. Model reduction step eliminates the least observable and controllable states by only retaining the states corresponding to larger Hankel singular values. So, by balanced truncation technique the states with small singular values are truncated. While following this process of model reduction it is important to keep the system input-output properties approximately same.

Each FPAA board from Anadigm family has limited number of op-amps and is capable of implementing only up to a maximum of eighth-order transfer function (for non-minimum phase systems, the realized order is even lesser). Hence, model reduction is a useful tool to be able to implement reduced order controller on a single FPAA hardware.

We now employ the control algorithms described in the previous section to the MFP-3D scanner Y-stage (and X-stage). As described earlier, the controllers were implemented on an FPAA system. Fig. 4.1 shows the experimental setup for controlling the nanopositioning system.

Feedback only  $H_\infty$  control design and three types of 2DOF control design described in the previous section are applied to the MFP-3D scanner. The plant transfer functions for the Y-stage and the X-stage are respectively,

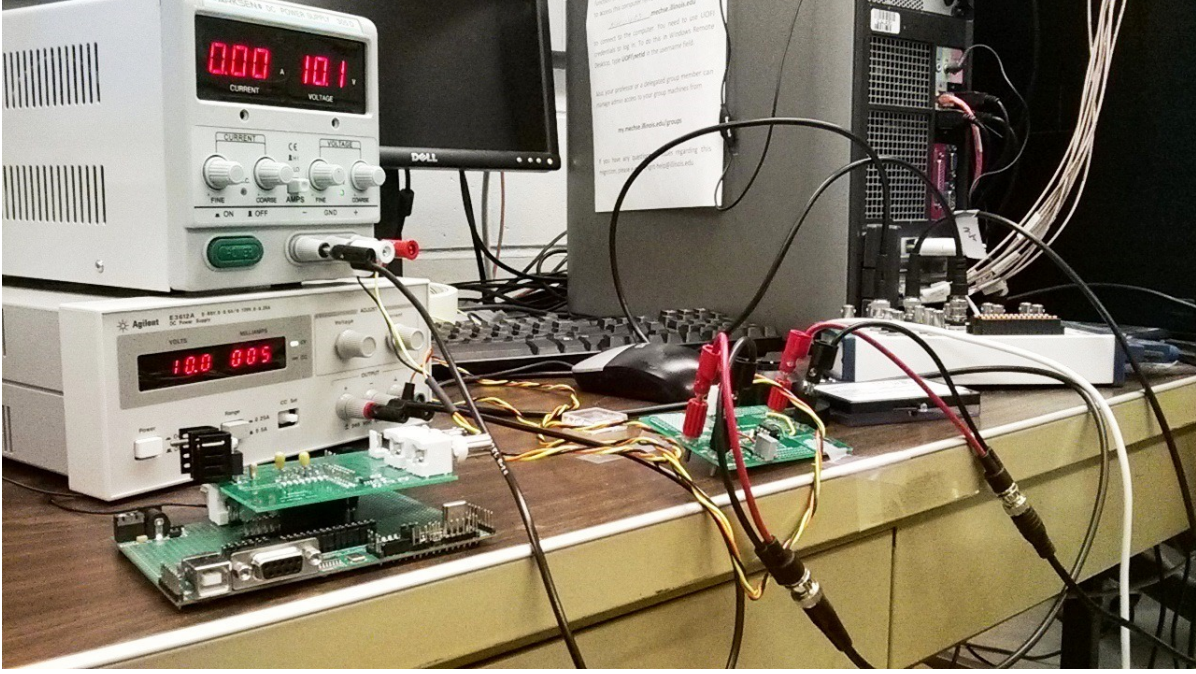


Figure 4.1: Experimental setup for controlling the nanopositioning system

$$\begin{aligned}
 G_{yy} &= \frac{0.025231(s + 1329)(s^2 + 1008s + 1.673 \times 10^7)}{(s + 738.8)(s^2 + 981.1s + 3.574 \times 10^6)} \\
 &\times \frac{(s^2 + 508s + 5.426 \times 10^7)(s^2 - 1.172 \times 10^4s + 1.097 \times 10^8)}{(s^2 + 1213s + 2.35 \times 10^7)(s^2 + 483.8s + 6.512 \times 10^7)} \quad (4.1.1)
 \end{aligned}$$

$$\begin{aligned}
 G_{xx} &= \frac{-0.022119(s + 2.954 \times 10^4)(s + 8117)(s - 8151)(s + 418.9)(s^2 + 890.2s + 1.131 \times 10^7)}{(s + 1796)(s + 217.1)(s^2 + 717.5s + 1.013 \times 10^7)(s^2 + 1827s + 3.751 \times 10^7)} \\
 &\times \frac{(s^2 + 1185s + 4.616 \times 10^7)(s^2 + 350.3s + 1.175 \times 10^8)(s^2 + 452.4s + 1.494 \times 10^8)}{(s^2 + 1440s + 7.142 \times 10^7)(s^2 + 267.1s + 1.182 \times 10^8)(s^2 + 605.8s + 1.473 \times 10^8)} \quad (4.1.2)
 \end{aligned}$$

## 4.2 1DOF $H_\infty$ control design

The  $H_\infty$  optimization routine was solved for the weighting functions  $W_s = \frac{0.5(s+1.257 \times 10^4)}{(s+125.7)}$ ,  $W_u = 0.1$ , and  $W_t = \frac{58.8235(s+1257)}{(s+1.257 \times 10^5)}$ . This optimization resulted in a ninth-order stable controller,  $K_{fb}$ , with  $\gamma_{opt} = 1.9183$ ,

$$\begin{aligned}
 K_{fb} &= \frac{0.0077965(s + 2096)(s + 1.257 \times 10^5)(s + 1.193 \times 10^9)}{(s + 2.605 \times 10^6)(s + 3.414 \times 10^4)(s + 125.7)} \\
 &\times \frac{(s^2 + 206.2s + 7.421 \times 10^5)(s^2 + 550.3s + 1.038 \times 10^7)(s^2 + 87.67s + 1.17 \times 10^7)}{(s^2 + 168.2s + 8.315 \times 10^5)(s^2 + 69.53s + 1.163 \times 10^7)(s^2 + 3544s + 2.199 \times 10^7)} \quad (4.2.1)
 \end{aligned}$$

Balanced truncation results in a reduced sixth-order controller given by,

$$K_{fb} = \frac{1.413(s + 3.607 \times 10^5)(s + 2150)(s^2 + 208.1s + 7.438 \times 10^5)(s^2 + 598.5s + 1.054 \times 10^7)}{(s + 3.972 \times 10^4)(s + 125.7)(s^2 + 168.7s + 8.335 \times 10^5)(s^2 + 3479s + 2.233 \times 10^7)} \quad (4.2.2)$$

The corresponding sensitivity and complementary sensitivity transfer functions are shown in the FIG. 4.2.

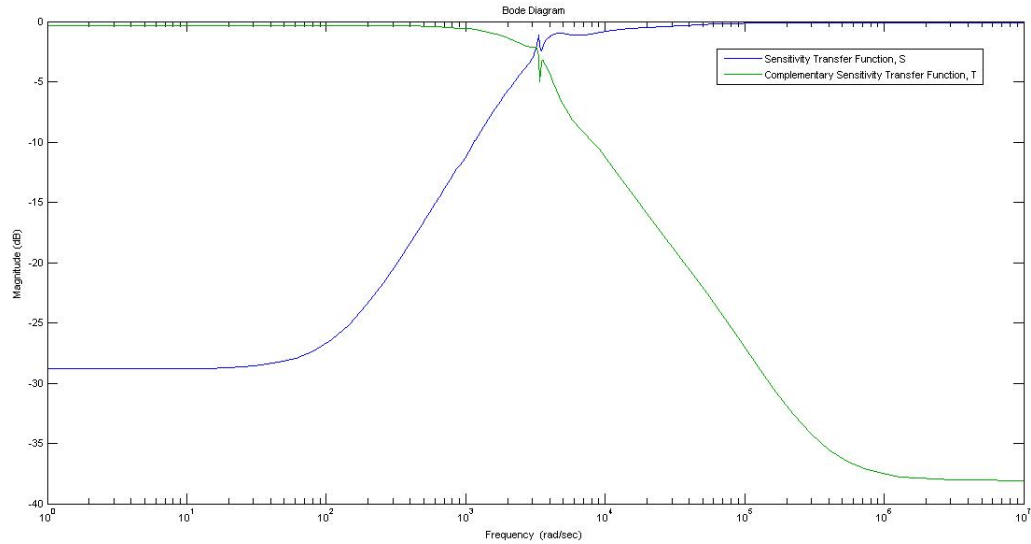


Figure 4.2: Theoretical  $S$  and  $T$  for 1DOF  $H_\infty$  control

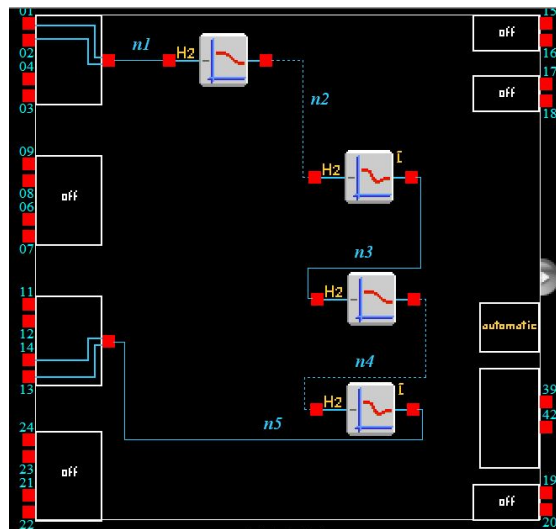
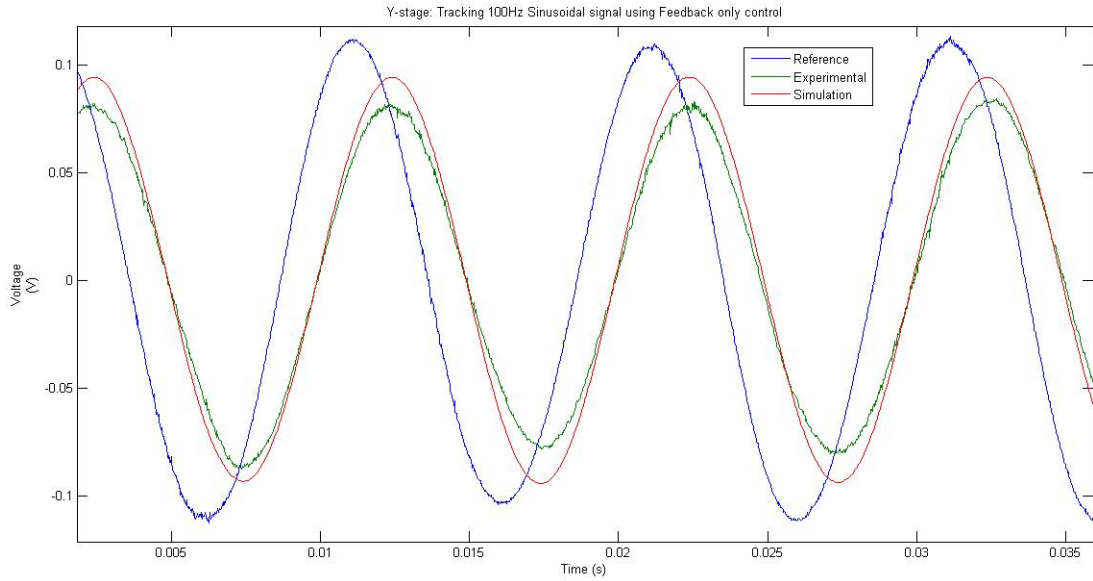
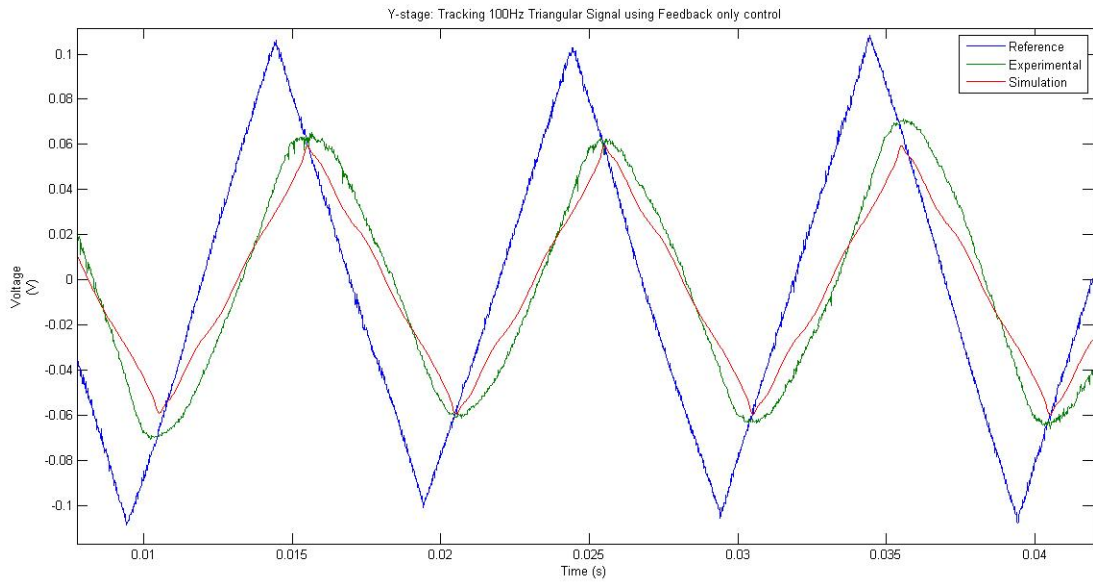


Figure 4.3: Designing reduced order feedback controller on an FPAA using AnadigmDesigner2 software

The experimental tracking results for 100Hz sinusoidal and triangular waveforms are shown in Fig. 4.4,



(a) Tracking a 100-Hz sinusoidal reference signal



(b) Tracking a 100-Hz triangular reference signal

Figure 4.4: Tracking performance using a 1DOF  $H_\infty$ -control design

From Fig. 4.2, the closed-loop bandwidth is approximately 280 Hz, which is a significant improvement in tracking bandwidth. The complementary sensitivity transfer function rolls-off at a rate of -20dB/decade, thereby, attenuating high-frequency noise.

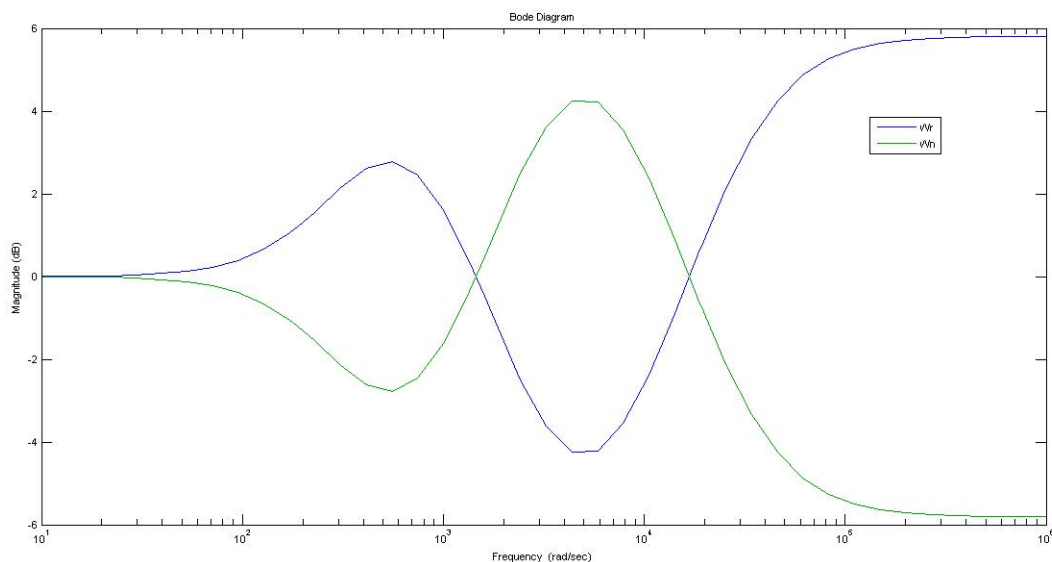


Figure 4.5: Choice of  $W_r$  and  $W_n$  weighting functions

### 4.3 2DOF $H_\infty$ control design

To overcome the shortcomings resulting from feedback only control, we now implement a 2DOF  $H_\infty$  control design. The performance objectives of high bandwidth, high resolution, and robustness to modeling errors are reflected into weighting transfer functions  $W_s$ ,  $W_u$  and  $W_t$ . Even though a 2DOF framework has separate controls for reference and error signals, the fundamental algebraic limitation still holds true,  $S + T = 1$ . To alleviate this problem even further, weighting functions  $W_r$  and  $W_n$  are used to shape reference and noise signals respectively. The weighting functions for the 2DOF optimization problem are:

$$W_s = \frac{0.5(s + 1.257 \times 10^4)}{(s + 125.7)} \quad (4.3.1)$$

$$W_u = 0.1 \quad (4.3.2)$$

$$W_t = \frac{58.8235(s + 1257)}{(s + 1.257 \times 10^5)} \quad (4.3.3)$$

$$W_r = \frac{1.9531(s + 251.3)(s + 5027)^2}{(s + 628.3)^2(s + 3.142 \times 10^4)} \quad (4.3.4)$$

$$W_n = W_r^{-1} \quad (4.3.5)$$

The choice of  $W_r$  and  $W_n$  is made such that at the frequency the  $W_t$  starts increasing,  $W_r$  starts increasing and  $W_n$  starts decreasing (in fact  $W_n$  is chosen as the inverse of  $W_r$ ). Fig. 4.5 shows the two weighting functions.

The optimization routine resulted in the feedforward controller,  $K_{ff}$  and feedback controller,  $K_{fb}$  with  $\gamma_{opt} = 2.8654$ . Model reduction technique resulted in the following reduced-order controllers,

$$K_{ff} = \frac{-2.2489(s + 1.706 \times 10^6)(s + 1.401 \times 10^4)(s + 6833)(s + 2790)(s - 6764)}{(s + 3.024 \times 10^5)(s^2 + 3052s + 4.001 \times 10^7)(s^2 + 1.798 \times 10^4s + 3.764 \times 10^8)} \quad (4.3.6)$$

$$K_{fb} = \frac{-0.66107(s + 1.217 \times 10^5)(s + 5.997 \times 10^5)(s - 9.831 \times 10^6)(s^2 + 405.5s + 3.445 \times 10^6)}{(s + 3.35 \times 10^5)(s + 1.219 \times 10^6)(s + 4.857 \times 10^4)(s + 1.08 \times 10^4)(s + 109.4)} \quad (4.3.7)$$

The experimental tracking results for 100Hz sinusoidal and triangular waveforms are shown in Fig. 4.7.

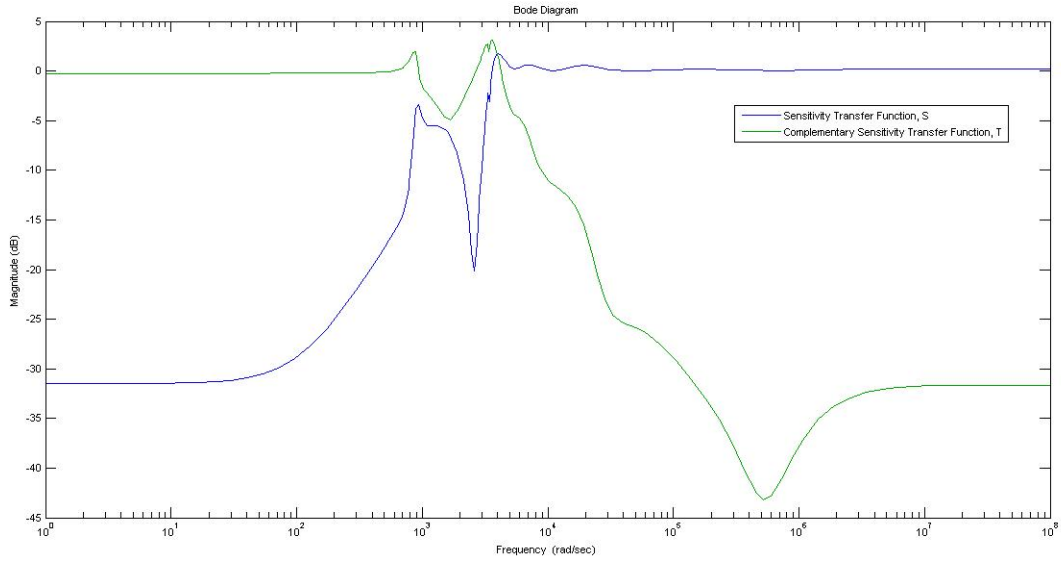
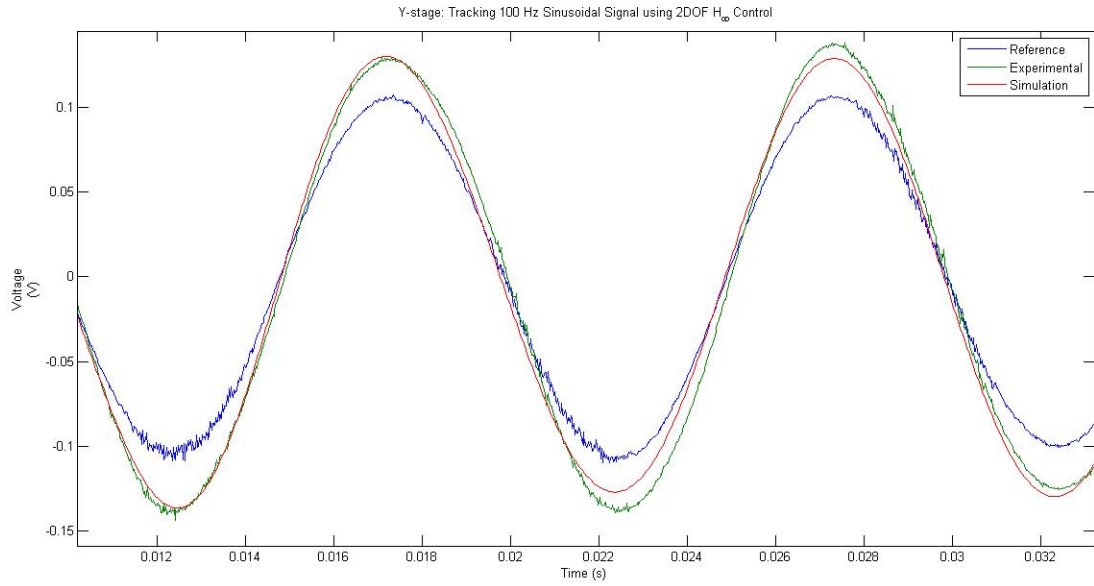
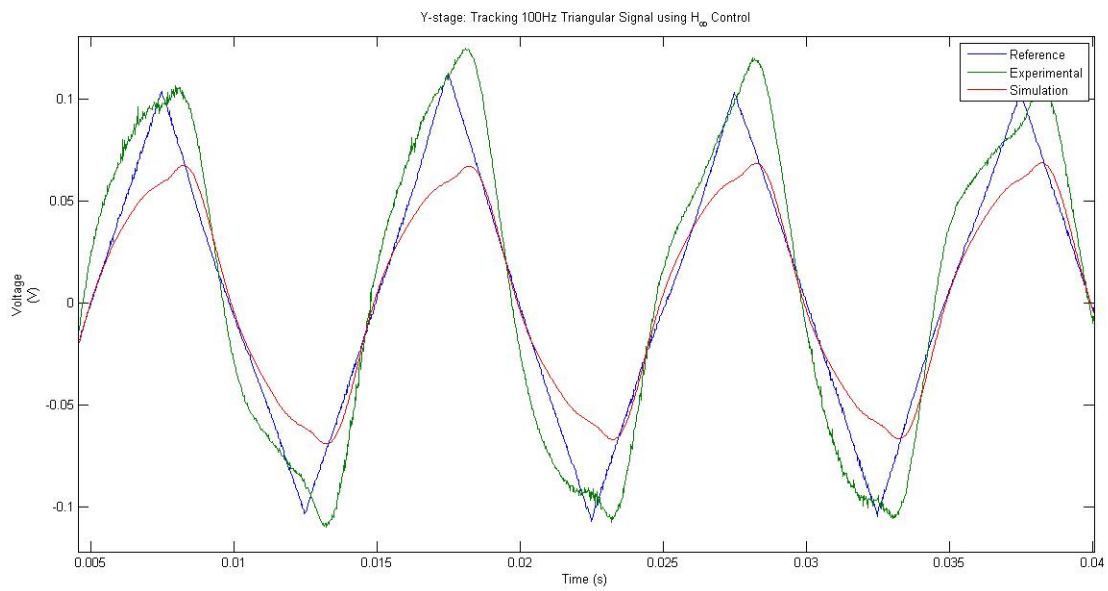


Figure 4.6:  $S$  and  $T$  for mixed-sensitivity 2DOF  $H_\infty$  control

Clearly, the 2DOF control design does a better job at tracking when compared to its 1DOF counterpart. The reference and experimental trajectories are in phase, whereas, this wasn't the case with 1DOF setup. From Fig. 4.6, the theoretical closed-loop bandwidth is approximately 490 Hz, which is a significant improvement in tracking bandwidth. The complementary sensitivity transfer function rolls-off at a rate of -20dB/decade, thereby, attenuating high-frequency noise.



(a) Tracking a 100-Hz sinusoidal reference signal



(b) Tracking a 100-Hz triangular reference signal

Figure 4.7: Tracking performance using a 2DOF  $H_\infty$ -control design

## 4.4 2DOF Model-Matching control

We now design the prefilter-based control, assuming  $K_{fb}$  as the pre-designed feedback component,

$$K_{fb} = \frac{-0.66107(s + 1.217 \times 10^5)(s + 5.997 \times 10^5)(s - 9.831 \times 10^6)(s^2 + 405.5s + 3.445 \times 10^6)}{(s + 3.35 \times 10^5)(s + 1.219 \times 10^6)(s + 4.857 \times 10^4)(s + 1.08 \times 10^4)(s + 109.4)} \quad (4.4.1)$$

The NP (Nevanlinna-Pick) solution resulted in a stable prefilter, which after model-reduction and dc gain adjustment resulted in the following sixth-order prefilter,

$$K_{pre} = \frac{0.00079405(s + 1.217 \times 10^6)(s + 2.804 \times 10^4)(s^2 + 428.6s + 9.935 \times 10^5)(s^2 + 1965s + 6.623 \times 10^6)}{(s^2 + 713.5s + 1.192 \times 10^6)(s^2 + 412s + 3.698 \times 10^6)(s^2 + 3286s + 4.048 \times 10^7)} \quad (4.4.2)$$

Fig. 4.8 shows the sensitivity and complementary transfer functions for the 2DOF model-matching control design. The theoretical bandwidth is roughly around 240Hz.

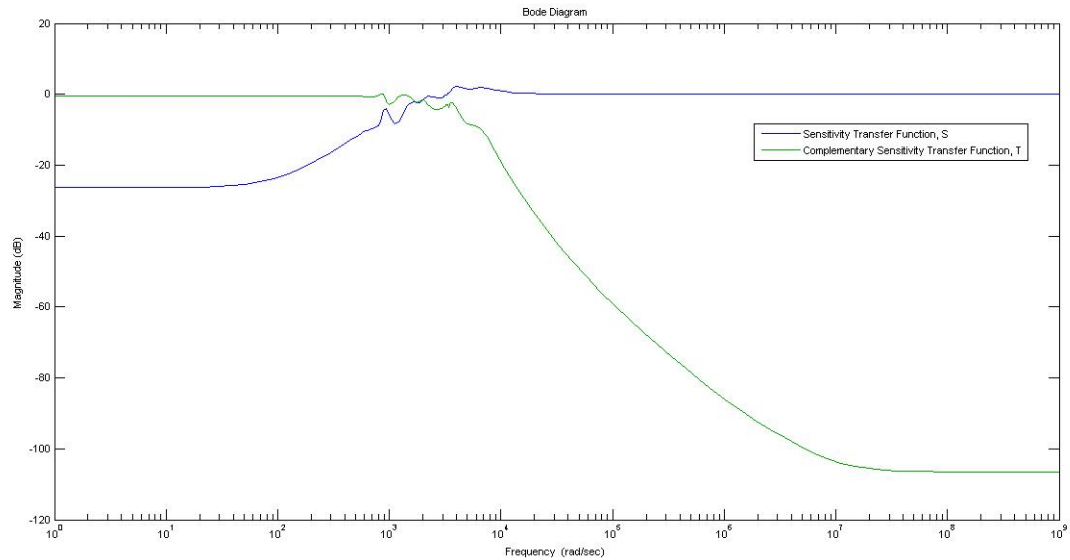
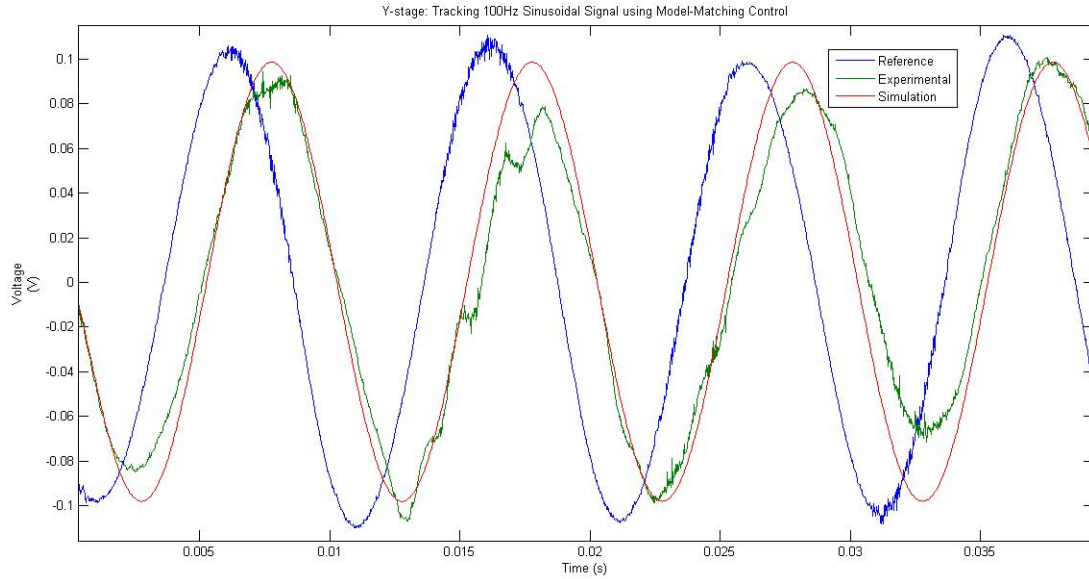
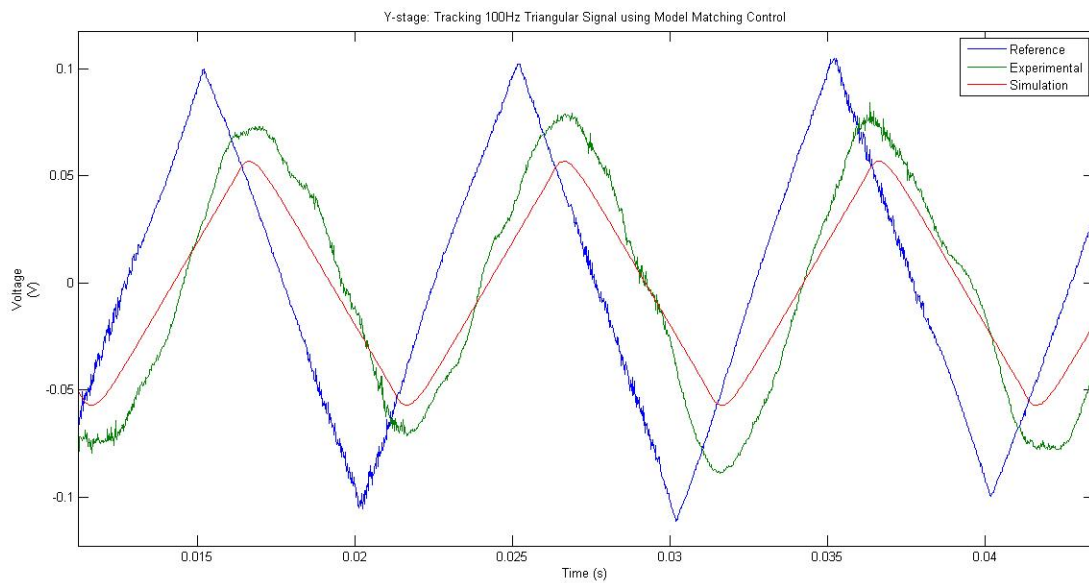


Figure 4.8:  $S$  and  $T$  for model-matching control

The experimental tracking results for 100Hz sinusoidal and triangular waveforms are shown in Fig. 4.9. The slightly poor tracking performance is attributed to the fact that the NP solution doesn't take into account the robustness properties of the closed-loop system.



(a) Tracking a 100-Hz sinusoidal reference signal



(b) Tracking a 100-Hz triangular reference signal

Figure 4.9: Tracking performance using a 2DOF optimal prefilter based design

## 4.5 2DOF Optimal Robust Model Matching control

An alternative representation of the 2DOF optimal robust model matching design is shown in the Fig. 4.10. where,  $W_1$  is the filter for shaping the plant  $G$ , and  $K_1$  is replaced by  $K_1 W_i$  to give exact model-matching at steady-state. The parameters,  $\rho$ ,  $W_1$  and  $T_{ref}$  can be adjusted, if required.

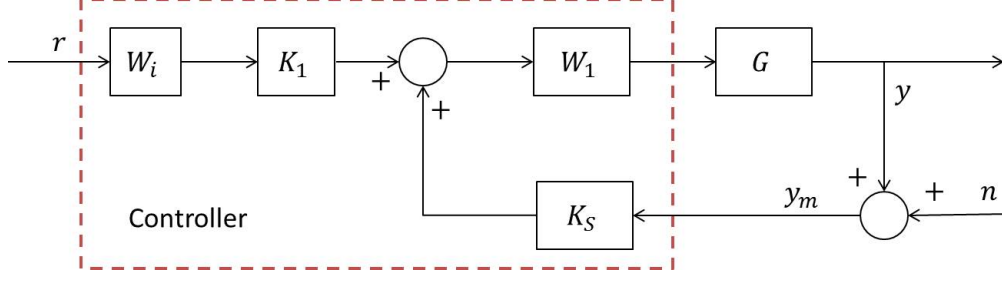


Figure 4.10:  $S$  and  $T$  for model-matching control

#### 4.5.1 Reduced-order controller for Y-stage

We now implement the above 2DOF  $H_\infty$  loop-shaping reduced-order controller on the Y-stage. With  $\rho = 1$  and  $W_1 = 1$ , the  $H_\infty$  optimization routine resulted in the following stabilizing controllers in the positive feedback setup,

$$K_1 = \frac{0.29483(s^2 + 223.4s + 7.538 \times 10^5)(s^2 + 536.7s + 1.063 \times 10^7)(s^2 + 6.262e04s + 1.063 \times 10^{10})}{(s + 7.195 \times 10^4)(s + 8701)(s^2 + 274.2s + 9.724 \times 10^5)(s^2 + 1959s + 1.179 \times 10^7)} \quad (4.5.1)$$

$$K_S = \frac{-0.051402(s + 5902)(s + 434.7)(s^2 - 1701s + 2.723 \times 10^6)}{(s^2 + 299.9s + 1.032 \times 10^6)(s^2 + 1651s + 1.386 \times 10^7)} \quad (4.5.2)$$

Fig. 4.11 shows the sensitivity and complementary transfer functions for the 2DOF model-matching control design. The theoretical bandwidth is roughly around 350Hz.

The experimental tracking results for 100Hz sinusoidal and triangular waveforms are shown in Fig. 4.14.

#### 4.5.2 High-order controller for X-stage

Till now, we had used only limited number of FPAA resources and were therefore not able to implement higher-order controllers. However, one can daisy chain two FPAA's together to implement higher-order transfer function. This is achieved by connecting the output of the one FPAA to the input of the other. We now implement higher-order 2DOF optimal robust model-matching controller for the X-stage, whose plant

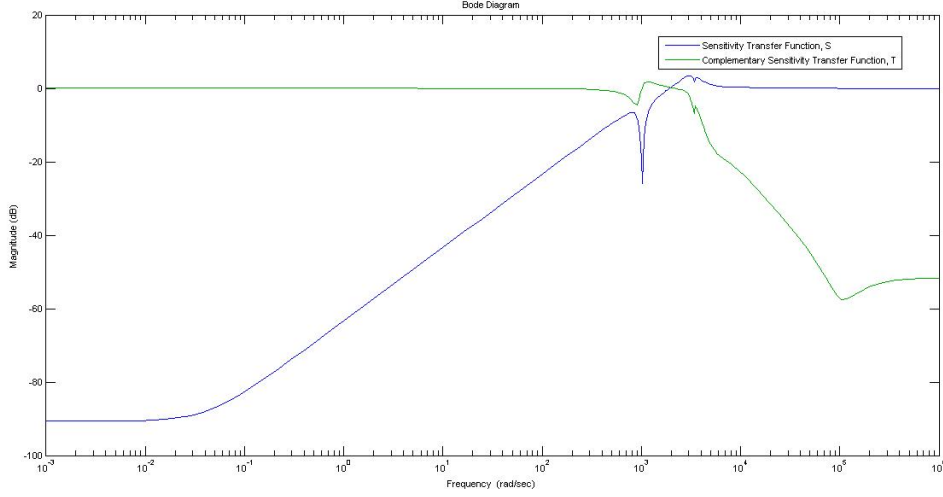


Figure 4.11:  $S$  and  $T$  for optimal robust 2DOF  $H_\infty$  loop-shaping controller for the Y-stage

transfer function is given by,

$$\begin{aligned}
 G_{xx} &= \frac{-0.022119(s + 2.954 \times 10^4)(s + 8117)(s - 8151)(s + 418.9)(s^2 + 890.2s + 1.131 \times 10^7)}{(s + 1796)(s + 217.1)(s^2 + 717.5s + 1.013 \times 10^7)(s^2 + 1827s + 3.751 \times 10^7)} \\
 &\times \frac{(s^2 + 1185s + 4.616 \times 10^7)(s^2 + 350.3s + 1.175 \times 10^8)(s^2 + 452.4s + 1.494 \times 10^8)}{(s^2 + 1440s + 7.142 \times 10^7)(s^2 + 267.1s + 1.182 \times 10^8)(s^2 + 605.8s + 1.473 \times 10^8)} \quad (4.5.3)
 \end{aligned}$$

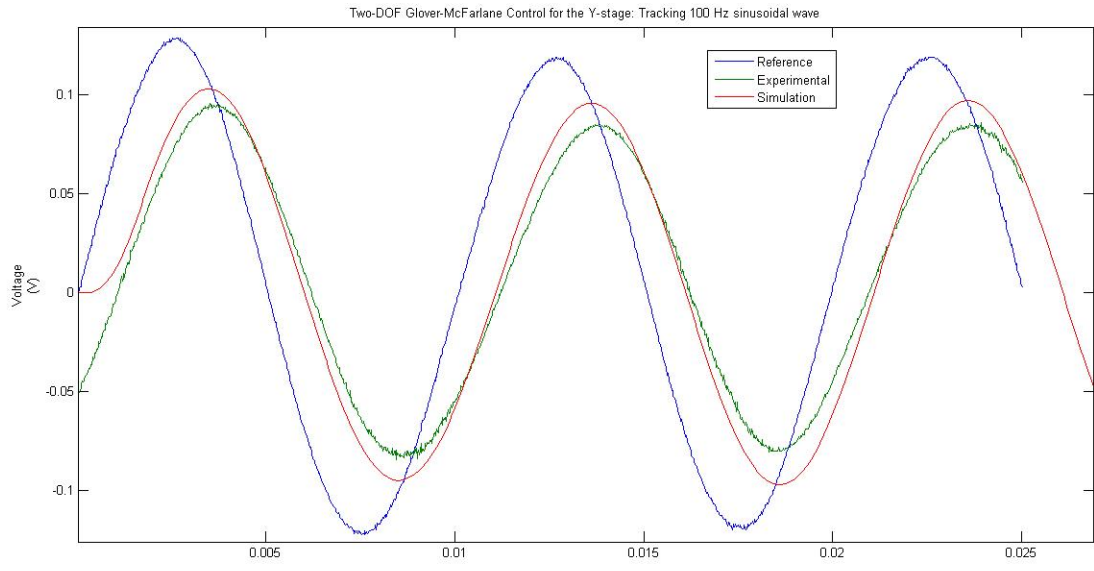
With  $\rho = 1$  and  $W_1 = 1$ , the  $H_\infty$  optimization routine resulted in the following stabilizing controllers in the positive feedback setup,

$$\begin{aligned}
 K_1 &= \frac{2473622.941(s + 1935)(s + 265.2)(s^2 + 750.2s + 1.031 \times 10^7)(s^2 + 1897s + 3.823 \times 10^7)}{(s + 1.087 \times 10^6)(s + 3336)(s + 481.3)(s^2 + 1035s + 1.117 \times 10^7)(s^2 + 9534s + 5.876 \times 10^7)} \\
 &\times \frac{(s^2 + 1740s + 7.089 \times 10^7)(s^2 + 285.9s + 1.168 \times 10^8)(s^2 + 588.7s + 1.471 \times 10^8)}{(s^2 + 1427s + 4.69 \times 10^7)(s^2 + 292.3s + 1.195 \times 10^8)(s^2 + 588.9s + 1.486 \times 10^8)} \quad (4.5.4)
 \end{aligned}$$

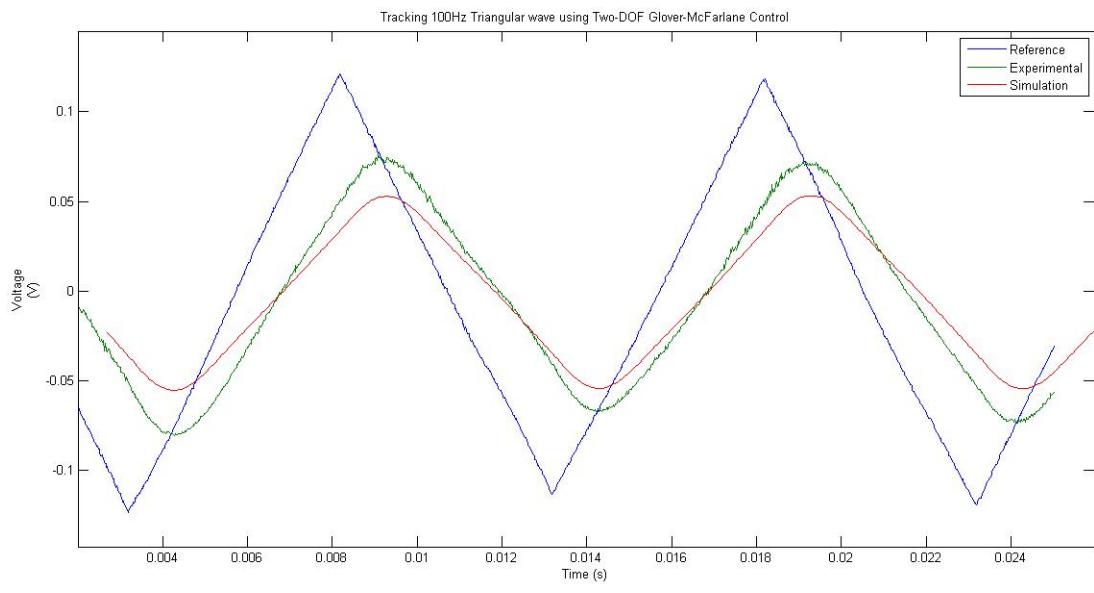
$$\begin{aligned}
 K_S &= \frac{0.044238(s - 8.466 \times 10^6)(s + 940.8)(s^2 + 682.2s + 8.254 \times 10^6)(s^2 + 944.6s + 3.15 \times 10^7)}{(s + 1.087 \times 10^6)(s + 482.4)(s^2 + 1032s + 1.109 \times 10^7)(s^2 + 9588s + 5.846 \times 10^7)} \\
 &\times \frac{(s^2 - 2520s + 5.961 \times 10^7)(s^2 + 201.2s + 1.181 \times 10^8)(s^2 + 637.9s + 1.47 \times 10^8)}{(s^2 + 1438s + 4.714 \times 10^7)(s^2 + 310.7s + 1.176 \times 10^8)(s^2 + 569.3s + 1.484 \times 10^8)} \quad (4.5.5)
 \end{aligned}$$

FPAAs implementation requires daisy chaining two FPAAs, as shown in the Fig. 4.13

The experimental tracking results for 100Hz sinusoidal and triangular waveforms are shown in Fig. 4.14.



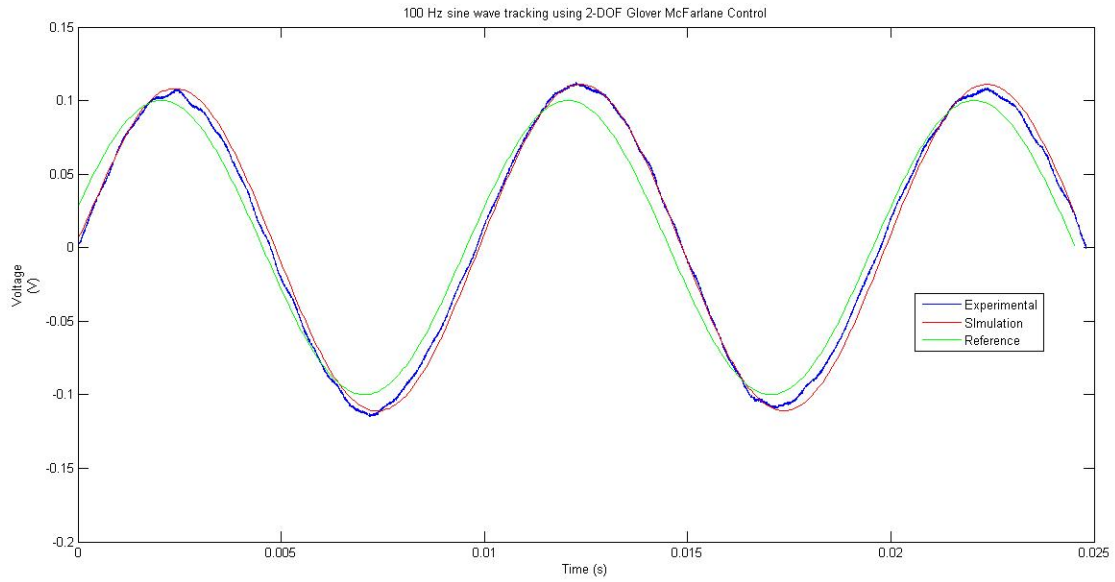
(a) Tracking a 100-Hz sinusoidal reference signal



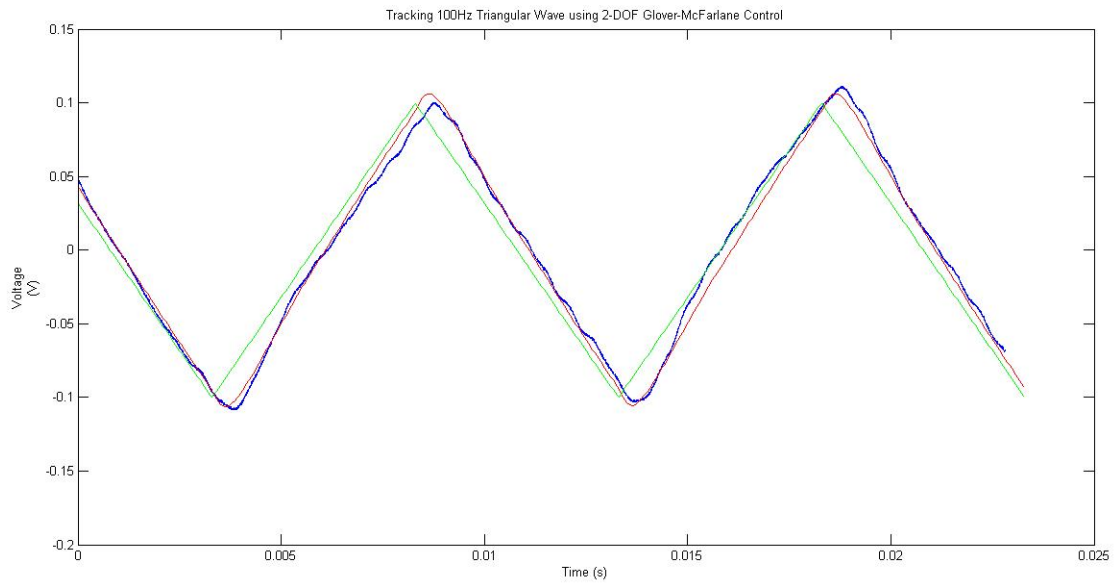
(b) Tracking a 100-Hz triangular reference signal

Figure 4.12: Tracking performance using a 2DOF optimal robust  $H_\infty$  loopshaping control for the Y-stage





(a) Tracking a 100-Hz sinusoidal reference signal



(b) Tracking a 100-Hz triangular reference signal

Figure 4.14: Tracking performance using a 2DOF optimal robust  $H_\infty$  loopshaping control for the X-stage

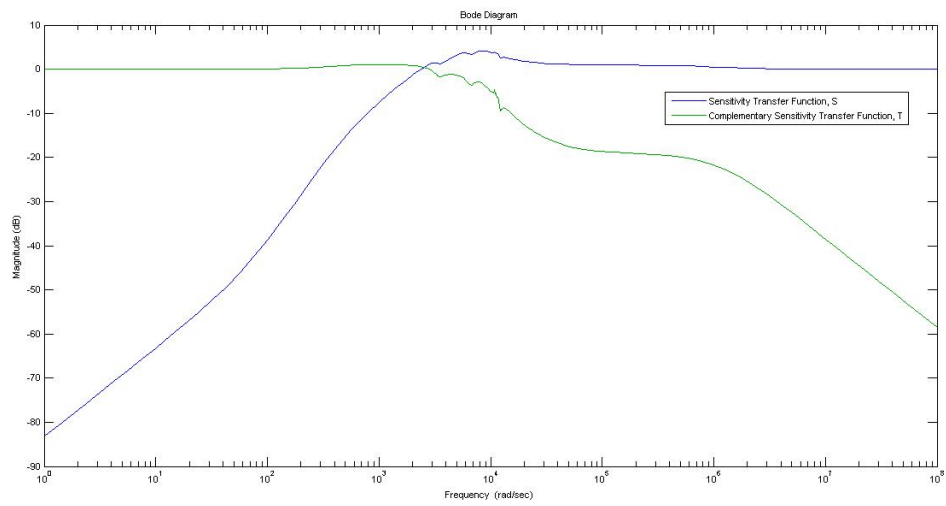


Figure 4.15:  $S$  and  $T$  for optimal robust 2DOF  $H_\infty$  loop-shaping controller for the X-stage

# Chapter 5

## Q-Control of Microcantilevers

### 5.1 Introduction

Having demonstrated the role of the FPAA's for the nanopositioning systems, it still remains to exploit their high-bandwidth ( $\sim 400kHz$ ) capabilities for the cantilever subsystem. A cantilever is a second-order flexible structure with very high resonant frequencies ( $10 - 400kHz$ ). Controlling a cantilever system will require hardware that can support similar bandwidth operations. In this chapter, we demonstrate the application of an FPAA system to the Q-control of microcantilevers. Moreover, we also demonstrate the FPAA's capabilities to perform other complex operations [8] such as, *multiplying two signals, sample and hold operation, sine wave generation, etc.*

For a similar image quality, a higher scan speed requires more information per time unit from the surface and therefore more interaction between tip and sample is needed. Stronger tip-sample interaction poses high Q-factor requirements on the cantilevers. Similarly, for rough/irregular samples with relatively larger feature sizes require cantilevers with reduced sensitivities and therefore, low Q-factor.

Also, it has been established that tapping mode yields good results when the lateral positioning bandwidths are about 1%-5% of the cantilever resonant frequencies. Increasing the resonance frequency of microcantilevers corresponding to increase in bandwidths of the positioning systems helps maintain the necessary ratio between the two frequencies and provides higher speed scans [35]. Hence, high positioning bandwidth ( $\sim 500Hz$ ) would mean higher cantilever resonant frequency ( $\sim 50kHz$ ). This poses high bandwidth requirements on the controller for performing Q-control.

## 5.2 Velocity estimation using modulation-demodulation approach

Cantilevers are second-order resonant structures with relatively sharper resonant frequencies (high Q-factor). A typical cantilever dynamics from piezo input to deflection can be approximated by the following ODE:

$$\ddot{x}(t) + \frac{\omega_n}{Q}\dot{x}(t) + \omega_n^2 x(t) = k\omega_n^2 u(t) \quad (5.2.1)$$

where,  $k$  is the DC gain.

In tapping mode AFM, the cantilevers are made to oscillate at frequencies close to the resonant frequencies. A typical cantilever tip deflection signal is oscillatory and is of the form,

$$x(t) = A \cos(\omega_0 t) + B \sin(\omega_0 t) \quad (5.2.2)$$

where,  $\omega_0 \approx \omega_n$  is the driving frequency of the cantilever.

Hence, the tip velocity is given by,

$$\begin{aligned} \dot{x}(t) &= -A\omega_0 \sin(\omega_0 t) + B\omega_0 \cos(\omega_0 t) \\ \frac{\dot{x}(t)}{\omega_0} &= -A \sin(\omega_0 t) + B \cos(\omega_0 t) \end{aligned} \quad (5.2.3)$$

Clearly, the cantilever tip velocity is orthogonal to the tip deflection signal. Hence, estimating tip velocity is equivalent to generating **orthogonal** signal to the given deflection signal.

Now, supposing we have correct estimate of the cantilever tip velocity, the corresponding piezo input for Q-factor control is given by:

$$u(t) = -K_v \frac{\dot{x}(t)}{\omega_0} + \hat{u}(t) \quad (5.2.4)$$

where,  $\hat{u}(t)$  can be used to control the cantilever's deflection

Substituting eq. 5.2.4 into cantilever dynamics, we obtain:

$$\ddot{x}(t) + \frac{\omega_n}{Q_{eff}}\dot{x}(t) + \omega_n^2 x(t) = k\omega_n^2 \hat{u}(t) \quad (5.2.5)$$

$$\text{where, } Q_{eff} = \frac{Q}{1 + kK_v Q} \quad (5.2.6)$$

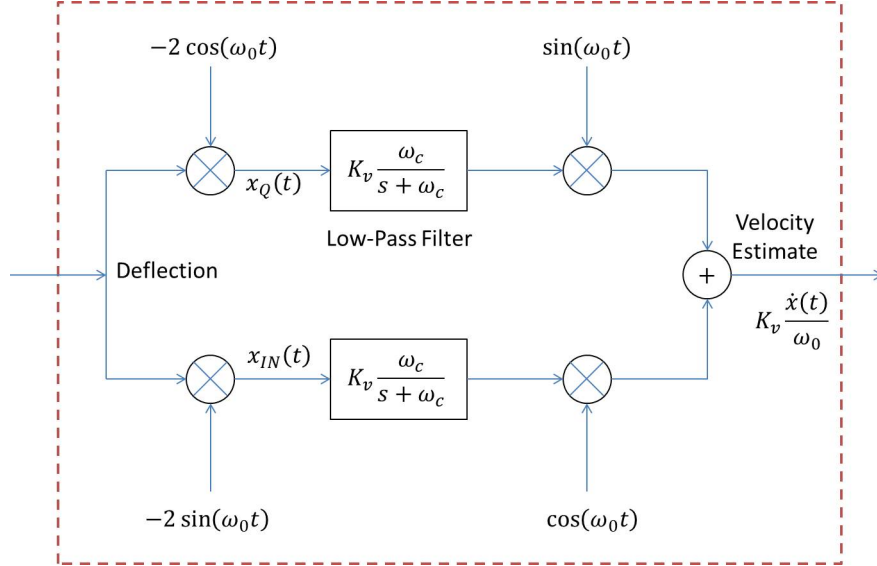


Figure 5.1: Schematic for velocity estimation

By choosing appropriate values (both positive and negative) for the gain parameter  $K_v$ , required Q-factors can be realized.

However, it still remains to correctly estimate the cantilever velocity. This is achieved by properly estimating the amplitudes  $A$  and  $B$  in eq. 5.2.2 using Modulation-Demodulation, a technique mostly used in radio transmissions. Fig. 5.1 shows the layout for velocity estimation using modulation-demodulation operation.

The deflection signal  $x(t)$  is multiplied by corresponding sinusoidal signals to obtain *in-phase* and *quadrature* components, as follows:

$$\begin{aligned}
 x_{IN}(t) = -2x(t) \sin(\omega_0 t) &= -2 \{A \cos(\omega_0 t) + B \sin(\omega_0 t)\} \sin(\omega_0 t) \\
 &= -A \sin(2\omega_0 t) - 2B \sin^2(\omega_0 t) \\
 &= -A \sin(2\omega_0 t) - B(1 - \cos(2\omega_0 t)) \\
 &= -B - A \sin(2\omega_0 t) + B \cos(2\omega_0 t)
 \end{aligned} \tag{5.2.7}$$

$$\begin{aligned}
x_Q(t) = -2x(t) \cos(\omega_0 t) &= -2 \{A \cos(\omega_0 t) + B \sin(\omega_0 t)\} \cos(\omega_0 t) \\
&= -2A \cos^2(\omega_0 t) - B \sin(2\omega_0 t) \\
&= -A(1 + \cos(2\omega_0 t)) - B \sin(2\omega_0 t) \\
&= -A - A \cos(2\omega_0 t) - B \sin(2\omega_0 t)
\end{aligned} \tag{5.2.8}$$

Clearly, the in-phase and quadrature components have not only DC components but sinusoidal components with resonant frequency  $2\omega_0$ . If we allow the individual signals to pass through a low pass filter  $F(s)$  with cut-off frequency  $\omega_c < 0.1\omega_0$ ,

$$F(s) = \frac{K_v \omega_c}{s + \omega_c} \tag{5.2.9}$$

The high-frequency component gets filtered out and the amplitudes  $A$  and  $B$  are recovered. The filtered signals are then multiplied by  $\sin(\omega_0 t)$  and  $-\cos(\omega_0 t)$  to obtain velocity estimate as:

$$\frac{\dot{x}_{est}(t)}{\omega_0} = -A \sin(\omega_0 t) + B \cos(\omega_0 t) \tag{5.2.10}$$

Clearly, the above equations is same as eq. 5.2.3.

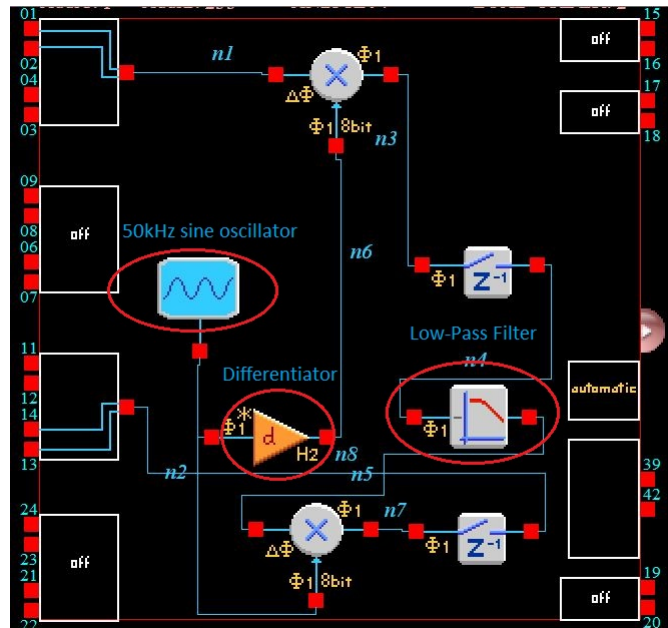


Figure 5.2: Implementing Modulation-Demodulation on FPAAs

### 5.3 Q-control implementation on FPAA and Experimental results

It's now evident from the previous section that implementing Q-control not only requires a low pass filter but also accurately generating two  $\frac{\pi}{2}$  phase-shifted oscillatory periodic waveforms and multiplying two high-frequency signals, too. Assuming that the cantilever driving frequency is roughly around 50kHz, a typical DSP (Digital Signal Processor) hardware is not suited for Q-control, as the Nyquist limit will require the hardware to support a minimum of 100kHz sampling frequency for all these operations. For better implementation, even higher sampling rate is required, i.e.,  $\sim 400kHz$  (corresponds to eight data points per cycle). This, however, can be easily achieved on an FPAA hardware, which has bandwidth up to 400kHz.

An FPAA implementation of this modulation-demodulation approach for a  $\sim 50kHz$  deflection signal is shown in the Fig. 5.2. The internal sine wave oscillator block is used to generate a 50kHz sinusoidal signal. The differentiator block then generates an equivalent 50kHz,  $\frac{\pi}{2}$  phase-shifted signal. The modulated signal is allowed to pass through a low-pass filter with cut-off frequency,  $f_C = 3kHz (\approx 0.06f_0)$ . The filtered signal is then multiplied by the phase-shifted signal. Two such FPAA boards are used to perform the two modulation-demodulation operations. The schematic of Q-control of the cantilever is shown in the Fig. 5.3

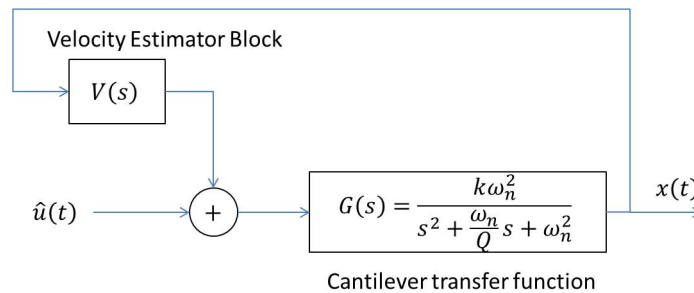


Figure 5.3: Schematic of Q-factor control of a microcantilever

Fig. 5.4 shows the experimental validation of this modulation-demodulation Q-control approach for a 50kHz deflection signal. Using this approach, we are able to generate an orthogonal signal of the same amplitude and frequency, thereby providing a reasonable estimate for velocity,

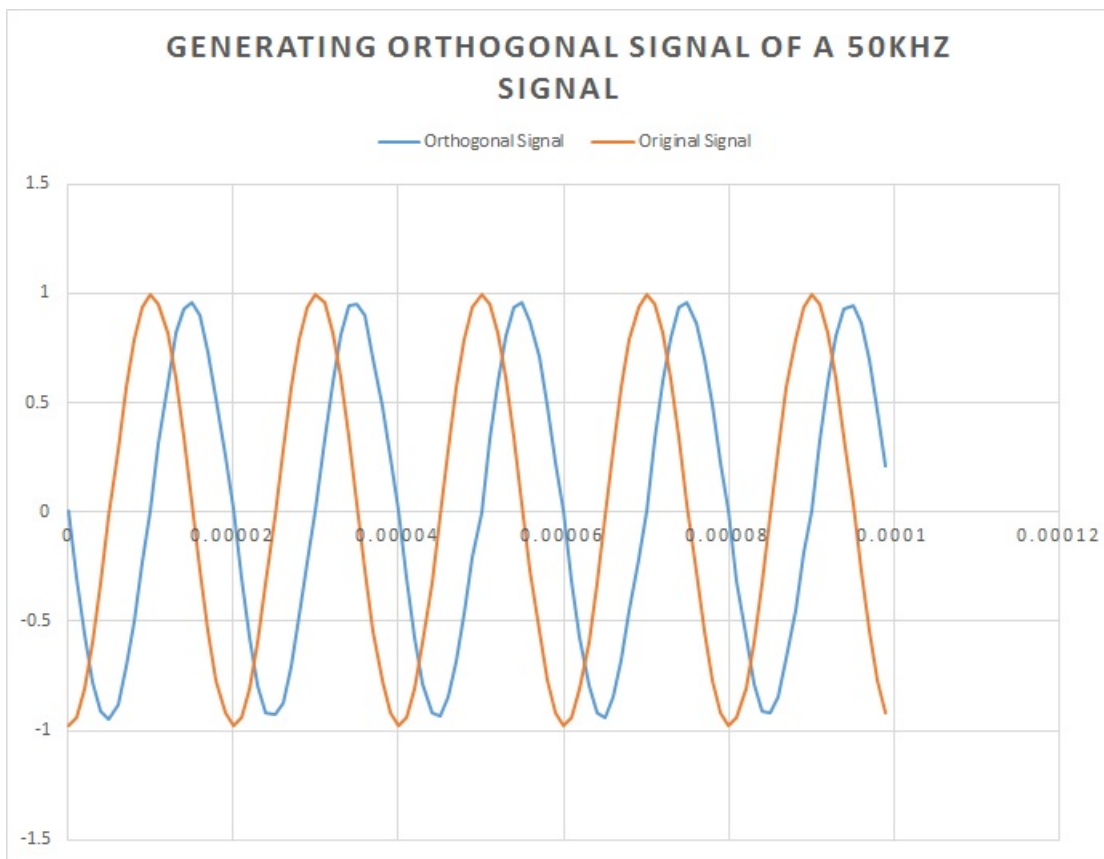


Figure 5.4: Estimating velocity using modulation-demodulation approach

## Chapter 6

# Conclusion and Future Work

The above work is a step towards the final goal of developing video-rate imaging in AFMs. This thesis highlights not only the significance of tools from the robust control theory to design high-bandwidth, high-resolution optimal control for nanopositioning systems, but also the direct implementation of these high-bandwidth controllers onto an FPAA, too. Three types of 2DOF control design (optimal prefilter model matching design, 2DOF mixed sensitivity synthesis, and 2DOF optimal robust model matching design) are described. The experimental results show a significant improvement in tracking bandwidth and match closely to the corresponding simulation results. With FPAAs, the achievable closed-loop nanopositioning system bandwidth is as high as 480 Hz, which is a significant improvement over the closed-loop bandwidth (300 Hz) achieved in [5, 10]. Moreover, a twelfth-order 2DOF  $H_\infty$  robust loop shaping controller for the X-stage results in high bandwidth, high resolution tracking performance as evident from the experimental results.

We plan to extend this work with FPAAs to develop a new mode of imaging that not only exploits the advantage with fast controllers to help achieve video-rate imaging, but also enable real-time property estimation. This will open up new avenues to imaging biological samples. Simulations pertaining to property estimation have been reported in [36]. We plan to exploit the capabilities of an FPAA to experimentally demonstrate real-time property estimation.

# References

- [1] S. Hauck and A. DeHon, *Reconfigurable computing: the theory and practice of FPGA-based computation*. Morgan Kaufmann, 2010.
- [2] S. Bains, “Analog’s answer to fpga opens field to masses,” *EE Times*, vol. 1510, p. 1, 2008.
- [3] J.-M. Galliere, “A control-systems fpaa based tutorial,” in *Proceedings of the 2nd WSEAS/IASME International Conference on Educational Technologies, Bucharest, Romania*, pp. 39–42, 2006.
- [4] N. Kodera, D. Yamamoto, R. Ishikawa, and T. Ando, “Video imaging of walking myosin v by high-speed atomic force microscopy,” *Nature*, vol. 468, no. 7320, pp. 72–76, 2010.
- [5] C. Lee and S. M. Salapaka, “Robust broadband nanopositioning: fundamental trade-offs, analysis, and design in a two-degree-of-freedom control framework,” *Nanotechnology*, vol. 20, no. 3, p. 035501, 2009.
- [6] G. Dullerud and F. Paganini, *Course in Robust Control Theory*. Springer-Verlag New York, 2000.
- [7] S. Skogestad and I. Postlethwaite, *Multivariable feedback control: analysis and design*, vol. 2. Wiley New York, 2007.
- [8] F. Anadigm, “Family overview,” *PDF File, Anadigm*, 2003.
- [9] T. Sulchek, R. Hsieh, J. Adams, G. Yaralioglu, S. Minne, C. Quate, J. Cleveland, A. Atalar, and D. Adderton, “High-speed tapping mode imaging with active q control for atomic force microscopy,” *Applied Physics Letters*, vol. 76, no. 11, pp. 1473–1475, 2000.
- [10] C. Lee, S. M. Salapaka, and P. G. Voulgaris, “Two degree of freedom robust optimal control design using a linear matrix inequality optimization,” in *Decision and Control, 2009 held jointly with the 2009 28th Chinese Control Conference. CDC/CCC 2009. Proceedings of the 48th IEEE Conference on*, pp. 714–719, IEEE, 2009.
- [11] S. Mashrafi, C. Preissner, S. Salapaka, and H. Zhao, “Something for (almost) nothing: X-ray microscope performance enhancement through control architecture change,” in *ASPE 28th Annual Meeting*, 2013.
- [12] S. M. Salapaka and M. V. Salapaka, “Scanning probe microscopy,” *Control Systems, IEEE*, vol. 28, no. 2, pp. 65–83, 2008.
- [13] G. Schitter and N. Phan, “Field programmable analog array (fpaa) based control of an atomic force microscope,” in *American Control Conference, 2008*, pp. 2690–2695, IEEE, 2008.
- [14] K. Glover and D. McFarlane, “Robust stabilization of normalized coprime factor plant descriptions with  $H_\infty$ -bounded uncertainty,” *Automatic Control, IEEE Transactions on*, vol. 34, no. 8, pp. 821–830, 1989.
- [15] Q. Zhong, D. Inness, K. Kjoller, and V. Elings, “Fractured polymer/silica fiber surface studied by tapping mode atomic force microscopy,” *Surface Science Letters*, vol. 290, no. 1, pp. L688–L692, 1993.

- [16] T. S. Hall, C. M. Twigg, P. Hasler, and D. V. Anderson, "Application performance of elements in a floating-gate fpa," in *Circuits and Systems, 2004. ISCAS'04. Proceedings of the 2004 International Symposium on*, vol. 2, pp. II-589, IEEE, 2004.
- [17] R. Selow, H. S. Lopes, and C. Lima, "A comparison of fpga and fpa technologies for a signal processing application," in *Field Programmable Logic and Applications, 2009. FPL 2009. International Conference on*, pp. 230-235, IEEE, 2009.
- [18] *Field Programmable Analog Array: AN231K04-DVLP3 - AnadigmApex Development Board*. Anadigm Inc., Campbell, CA, USA, 2006.
- [19] L. Ljung, "System identification: theory for the user," *Prentice Hall Int and System Sciences Series, New Jersey*, vol. 7632, 1987.
- [20] G. Mohan, *A new dynamic mode for fast imaging in atomic force microscopes*. PhD thesis, University of Illinois at Urbana-Champaign, 2013.
- [21] D. Croft, G. Shed, and S. Devasia, "Creep, hysteresis, and vibration compensation for piezoactuators: atomic force microscopy application," *Journal of Dynamic Systems, Measurement, and Control*, vol. 123, no. 1, pp. 35-43, 2001.
- [22] A. G. Hatch, R. C. Smith, T. De, and M. V. Salapaka, "Construction and experimental implementation of a model-based inverse filter to attenuate hysteresis in ferroelectric transducers," *Control Systems Technology, IEEE Transactions on*, vol. 14, no. 6, pp. 1058-1069, 2006.
- [23] B. Bhikkaji, M. Ratnam, A. J. Fleming, and S. R. Moheimani, "High-performance control of piezoelectric tube scanners," *Control Systems Technology, IEEE Transactions on*, vol. 15, no. 5, pp. 853-866, 2007.
- [24] A. Daniele, S. Salapaka, M. Salapaka, and M. Dahleh, "Piezoelectric scanners for atomic force microscopes: Design of lateral sensors, identification and control," in *American Control Conference, 1999. Proceedings of the 1999*, vol. 1, pp. 253-257, IEEE, 1999.
- [25] S. Salapaka, A. Sebastian, J. P. Cleveland, and M. V. Salapaka, "High bandwidth nano-positioner: A robust control approach," *Review of scientific instruments*, vol. 73, no. 9, pp. 3232-3241, 2002.
- [26] K. K. Leang and S. Devasia, "Hysteresis, creep, and vibration compensation for piezoactuators: Feedback and feedforward control," in *Proceedings of the Second IFAC Conference on Mechatronic Systems, Berkeley, CA, Dec*, pp. 9-11, 2002.
- [27] G. Schitter, F. Allgöwer, and A. Stemmer, "A new control strategy for high-speed atomic force microscopy," *Nanotechnology*, vol. 15, no. 1, p. 108, 2004.
- [28] Q. Zou and S. Devasia, "Preview-based optimal inversion for output tracking: Application to scanning tunneling microscopy," *Control Systems Technology, IEEE Transactions on*, vol. 12, no. 3, pp. 375-386, 2004.
- [29] J. C. Doyle, B. A. Francis, and A. Tannenbaum, *Feedback control theory*, vol. 1. Macmillan Publishing Company New York, 1992.
- [30] A. Sebastian and S. M. Salapaka, "Design methodologies for robust nano-positioning," *Control Systems Technology, IEEE Transactions on*, vol. 13, no. 6, pp. 868-876, 2005.
- [31] D. McFarlane and K. Glover, "A loop-shaping design procedure using  $H_\infty$  synthesis," *Automatic Control, IEEE Transactions on*, vol. 37, no. 6, pp. 759-769, 1992.
- [32] D. Hoyle, R. Hyde, and D. Limebeer, "An  $H_\infty$  approach to two degree of freedom design," in *Decision and Control, 1991., Proceedings of the 30th IEEE Conference on*, pp. 1581-1585, IEEE, 1991.

- [33] D. J. Limebeer, E. Kasenally, and J. Perkins, “On the design of robust two degree of freedom controllers,” *Automatica*, vol. 29, no. 1, pp. 157–168, 1993.
- [34] M. Vidyasagar, *Control system synthesis: a factorization approach*. Morgan & Claypool Publishers, 2011.
- [35] D. Walters, J. Cleveland, N. Thomson, P. Hansma, M. Wendman, G. Gurley, and V. Elings, “Short cantilevers for atomic force microscopy,” *Review of Scientific Instruments*, vol. 67, no. 10, pp. 3583–3590, 1996.
- [36] S. M Salapaka, T. De, and A. Sebastian, “A robust control based solution to the sample-profile estimation problem in fast atomic force microscopy,” *International Journal of Robust and Nonlinear Control*, vol. 15, no. 16, pp. 821–837, 2005.